Oxygen electrodes for ceramic fuel cells with proton and oxide ion conducting electrolytes

Ragnar Strandbakke

Dissertation for the degree of Philosphiae Doctor

Department of Chemistry

Faculty of Mathematics and Natural Sciences

UNIVERSITETY OF OSLO

2014

Preface

This dissertation is part of the work for the degree of Philosophiae Doctor (PhD) at Department of Chemistry, Faculty of Mathematics and Natural Sciences, University of Oslo, Norway. The work has been carried out at the Centre for Materials Science and Nanotechnology (SMN) at the Group for Solid State Electrochemistry under the supervision of Professors Truls Norby and Reidar Haugsrud in the period August 2008 to July 2014.

It is with heartfelt gratitude I thank my main supervisor Professor Truls Norby for the incisive guidance given throughout the whole working period. The guidance has possibly been accompanied by a vague hope of disproving the old saying about learning the old dog how to sit, and hopefully the effort has paid some dividends. I also want to thank my co-supervisor Professor Reidar Haugsrud for our many valuable discussions and for being such a patient source of knowledge next door.

Many thanks must also be given to the Group for Solid State Electrochemistry. I have been most fortunate to be surrounded by such a group of resourceful and social colleagues. Especially the joint efforts of digging into the electrode mysteries, shared with Dr. Vasilis Besikiotis, the discussions and collaborations with "office co-habitant and door-opener" Dr. Anna Magrasó and the more philosophical and profound activities shared with Drs Zuoan Li and Harald Malerød-Fjeld.

But most of all my thanks go to my dearest family, Monica Ilni, Katharina and Mattis. Through many years of master and PhD work you have patiently waited with late dinners, raised your eyebrows over an absent-minded father / husband, taken care of me and each other and listened to all sorts of strange concepts beyond any grasp. At least you now know more about fuel cells than most people. Thank you!

Summary

The overall aim of this work is to contribute to a better understanding of the reactions taking place at the oxygen electrode in proton ceramic fuel cells (PCFCs) and, moreover, to develop new materials with improved performance for this electrode. PCFCs and their cathode reactions are the main focus of the study, but these reactions are often running in parallel with reactions associated with other charge carriers that also need to be addressed. Most proton conducting ceramics exhibit also transport of oxide ions, and although small at intermediate temperatures, the relative contribution from partial oxide ion conductivity increases with temperature and eventually dominates at higher temperatures. Hence, characterization of the performance of a PCFC cathode may at higher temperatures in reality be affected by or even directly reflect the cathode reactions of an oxide ion conducting solid oxide fuel cell (SOFC) rather than that of a PCFC. The crossover between SOFCs and PCFCs with respect to the oxygen electrode reactions is emphasized in this work.

The first manuscript presents status and challenges of PCFC research undertaken in Norway by the start of 2010. The work comprises manufacturing of single cells and cell stacking, focusing on the performance, the mechanical and thermal properties, as well as, the chemical stability of the different PCFC component materials. State-of-the-art cathode material at that time, $La_{0.8}Sr_{0.2}MnO_3$ (LSM), showed a polarization resistance (R_p) of 30 Ωcm^2 at 800°C on proton conducting Ca doped $LaNbO_4$ electrolyte, revealing the necessity for a significant improvement in the cathode performance. New materials had to be found and their microstructural design optimized, based on the requirements specific for the proton conductor oxygen reaction.

Reaction kinetics, with particular emphasis on the features specific for the PCFC oxygen electrode is investigated in manuscripts II, III and V. In manuscript IV, the experimental conditions are such that the SOFC reactions dominate the electrode process. The electrolyte/electrode interfacial exchange of protons instead of oxide

ions distinguishes PCFCs from oxide ion conducting SOFCs and entails that water is formed on the oxygen side of the electrolyte. A major challenge with the PCFC cathode candidate materials studied so far is the confinement of the electrochemical process to pass the electrolyte / electrode / gas triple phase boundary (tpb), instead of utilizing the whole electrode area as for the best mixed conducting SOFC electrodes. The challenges related to tpbs as a bottleneck are addressed by microstructural improvements. Moreover, a novel material with simultaneous transport of electrons and protons is introduced that will enable also the PCFC cathode reactions to occur over the electrode surface, thereby extending the tpb reaction zone.

The effect of water formation on the cathode reaction is studied in detail on a Pt model electrode. The results show higher reaction rates upon increased water vapor partial pressure, pH_2O. Since the Pt electrode is rate limited by surface diffusion both under dry and wet conditions, the pH_2O effect is explained by the formation of surface hydroxyls with high surface mobility relative to the adsorbed oxide ions which dominate under drier conditions. The presence of surface hydroxyls is confirmed by X-ray photoelectron spectroscopy. Water is looped in the oxygen reaction series, acting both as reactant and product. In manuscript V and in the results part of the thesis it is shown that ambient water vapor gives the same positive effect for the mixed conducting electrodes $BaGd_{0.8}La_{0.2}Co_2O_{6-\delta}$ (BGLC) and $BaPrCo_2O_{6-\delta}$ (BPC) when operated on a $BaZr_{0.7}Ce_{0.2}Y_{0.1}O_3$ (BZCY72) proton conducting electrolyte. At higher temperatures where BZCY72 is mainly oxide ion conducting, water vapor on the other has an adverse effect on the electrode reaction rate for the same mixed conducting electrodes. With the mixed oxide ion-p-type electron conductor $La_2NiO_{4+\delta}$ (LNiO) as electrode and $La_{27.16}W_{4.85}O_{55.27}$, (La/W ≈ 5.6; LWO56) as electrolyte (manuscript IV), the electrode performance was independent of pH_2O under conditions where oxide ion conductivity dominates in the electrolyte (above 700°C).

Three well-established routes to improve the electrode microstructure were followed in this work; (i) addition of nano-sized catalysts by infiltration, (ii) improvement of the functional layer close to the electrolyte and (iii) manufacturing of

composite electrodes by mixing electrode and electrolyte materials. The two first methods showed promising results: Addition of Pt nanoparticles in the LSM electrode lowered significantly the polarization resistance; from 260 to 40 Ωcm^2 at 650°C. Characterization of the microstructure of BGLC and BPC electrodes showed that a fine-grained functional layer was successfully manufactured. The composite electrode approach did, however, not prove to enhance the performance of an electrode rate limited by surface reactions.

The materials investigated in this work range from well-known pure electron conductors such as Pt and LSM, used first and formerly for the detailed characterization of the electrode reactions, via the promising mixed conducting candidate LNiO, to the novel mixed conducting double perovskites BGLC, BPC and their B-site iron-substituted variants $BaGdCo_{1.8}Fe_{0.2}O_{6-\delta}$ (BGCF) and $BaPrCo_{1.4}Fe_{0.6}O_{6-\delta}$ (BPCF). For Pt and LSM, high capacitance processes like surface diffusion is limiting the overall electrode reaction rate. For the mixed conducting electrodes LNiO and BGLC, the oxide ion transfer is shown to happen through the electrode interior. The latter also shows indications of partial bulk proton conductivity concluded based on the pH_2O dependencies encountered for R_p and supported by hydration of the material at low temperatures with a hydration enthalpy of -50 kJ/mol. Bulk proton transport would facilitate the low temperature PCFC cathode reaction and widen the triple phase reaction zone improving the electrode performance. The behavior of these mixed conducting double perovskites, especially BGLC but possibly also BPC, with polarization resistances measured to 0.05 and 0.09 Ωcm^2 at 650°C for BGLC and BPC, consequently gives indications of the first established mixed proton / electron conducting materials with sufficient electrochemical performance on a proton conducting electrolyte.

To account correctly for mixed conductivity in the electrolyte is challenging when studying electrode reactions. In manuscript III and V, a model for the separation of the measured polarization resistance into the contributions from more than one charge carrier is developed. The model accounts also for the effect of parallel non-faradaic current during high temperature measurements under oxidizing

conditions. The results of the modelling show that the measured polarization resistance for the system investigated here and reported above for 650°C is underestimated by approximately one order of magnitude. The same underestimation would apply to any other oxygen electrode measured on BZCY72 if the effect of electrolyte p-type partial conductivity was not properly addressed. In a running fuel cell or electrolyzer cell, the fuel-side reducing conditions are expected to induce a blocking layer for electronic conductivity in the electrolyte. The "true" polarization resistance will therefore be higher when the partial short circuit is absent. At lower temperatures, this effect of parallel non-faradaic current is less pronounced during half-cell electrode characterization.

BGLC exhibits a total polarisation resistance for proton transport of only 10 Ωcm^2 at 350°C, with an activation energy of 50 $kJmol^{-1}$ ascribed mainly to the surface electrode reaction. Based on this, there is reason to believe that further improvements of the cathode performance can be achieved by enhanced microstructural processing, such as infiltration of BGLC in a BZCY backbone.

List of symbols and abbreviations

PCFC: Proton ceramic fuel cell

SOFC: Solid oxide fuel cell

LSM: $La_{0.8}Sr_{0.2}MnO_3$

R: Resistance

R_p: Polarization resistance

$R_{el.l}$: Electrolyte resistance

R_{ion}: ionic resistance

R_{el}: Electronic resistance

tpb: Triple phase boundary

BGLC: $BaGd_{0.8}La_{0.2}Co_2O_{6-\delta}$

BPC: $BaPrCo_2O_{6-\delta}$

BZCY72: $BaZr_{0.7}Ce_{0.2}Y_{0.1}O_3$

LNiO: $La_2NiO_{4+\delta}$

LWO56: $La_{27.16}W_{4.85}O_{55.27}$

BGCF: $BaGdCo_{1.8}Fe_{0.2}O_{6-\delta}$

BPCF: $BaPrCo_{1.4}Fe_{0.6}O_{6-\delta}$

CHP: Combined heat and power

YSZ: Yttria-stabilized zirconia

ASR: Area specific resistance

O-MIEC: Mixed oxide ionic / electronic conductor

SSC: $Sm_{0.5}Sr_{0.5}CoO_3$

BSCF: $Ba_{0.5}Sr_{0.5}Co_{0.8}Fe_{0.2}O_{3-\delta}$

LSCF: $La_{0.6}Sr_{0.4}Co_{0.2}Fe_{0.8}O_{3-\delta}$

P-MIEC: Mixed protonic / electronic conductor

BPC: $PrBaCo_2O_{5+\delta}$

PNO: Pr_2NiO_4

$Mf_M^{/}$: Foreign, -1 effectively negatively charged metal dopant

$v_O^{\bullet\bullet}$: +2 effectively positively charged oxygen vacancy

n: In defect chemistry: Concentration of defect electrons. In impedance spectroscopy: CPE parameter

p: Concentration of defect electron holes

K_n: Equilibrium constant for the formation of electrons

K_p: Equilibrium constant for the formation of electron holes

K_{Hydr}: Equilibrium constant for the formation of proton defects by hydration

σ : Conductivity

z : Charge

e : Elementary charge

c : Concentration

μ : In transport: Mobility. In electrochemistry: Chemical potential

d_m: Molar density

E_A: Activation energy

φ: Electric potential

$\tilde{\mu}$: Electrochemical potential

F: Faraday's constant

a: Activity

k: In electrode kinetics: Reaction rate constant. In impedance spectroscopy: Chemical parameter of Gerischer element

k^+: Forward reaction rate constant

k^-: Reverse reaction rate constant

E_F : Fermi energy

E_{Ox}^0 : Energy of oxidized adsorbate molecule orbital most likely to be occupied by transferred electron

E_{red} : Reduction potential

η: Overpotential

R: Universal gas constant

T: Temperature (K)

r: Reaction rate

i: Current density

α: Anodic symmetry coefficient

β: Cathodic symmetry coefficient

d: Diffusion

ct: Charge transfer

SDC: $Ce_{0.8}Sm_{0.2}O_{2-\delta}$

BCS: $BaCe_{0.8}Sm_{0.2}O_{3-\delta}$

C: Capacitance

EIS: Electrochemical impedance spectroscopy

θ: Phase shift

Z: Impedance

j: Imaginary number

ω: Angular frequency

U: Voltage

I: Current

τ: Time constant

CPE: Constant phase element

Y_0: In CPE: Capacitance parameter. In Gerischer element: Admittance parameter

PCEC: Proton ceramic electrolyzer cell

Contents

1.   **Introduction**

US Department of Energy released in 2009 their technical and cost targets for the development of energy production based on fuel cells: Within 2015, the efficiency for combined heat and power (CHP) should reach 87.5 %, with 40 % being electrical efficiency and with a lifetime of 40,000 hrs, for 1-10 kW residential fuel cell systems running on natural gas. Status in 2008 was 80 % efficiency (34 % electrical) and 6000 hrs lifetime. CHP demands high temperature systems causing challenges with degradation. This is particularly demanding, as also reflected in the large discrepancy between the 2008 status and 2015 targeted lifetime [1]. The fuel cell research is still striving towards the 2009 targets, and in 2012, almost 1000 fuel cell related patents were issued in the US alone - more than for any other clean energy technology including solar. This clearly shows that fuel cell research is proceeding with full momentum.

The 2008 state-of the-art SOFC was based on oxide-ion conducting yttria-stabilized zirconia (YSZ) as electrolyte. Its operation temperature is 800-1000°C, and even though YSZ-based systems show high CHP efficiency, the high operation temperature causes severe degradation problems: High temperature seals degrade upon thermal cycling, interconnect materials, such as the ceramic $La_{1-x}Ca_xCrO_3$, subjected to dual atmospheres and ambient water at high temperatures suffer from growth of oxide scales, and electrodes are easily poisoned by volatile interconnect elements such as Cr-containing species. Therefore, lowering the operation temperature is desirable, allowing for the use of ferritic stainless steel interconnect materials and glass seals.

The relatively high activation energy for oxide ion transport in the YSZ electrolyte limits the possibility to decrease the operating temperature with this electrolyte and YSZ is generally replaced with intermediate temperature ionic conductors such as acceptor doped CeO_2 and $LaGaO_3$-based materials [2]. However, a stable, combined area specific resistance (ASR) for anode, electrolyte and cathode

below 0.5 Ωcm^2 with sufficient operation lifetime is challenging to reach at intermediate temperatures.

1.1 Background

Proton ceramic fuel cells with proton conducting electrolyte materials present a good alternative to the oxide ion conducting SOFCs at intermediate temperatures. Transport of protons generally shows lower activation energy than for oxide ions [3], and proton conductors thus potentially have higher conductivity at lower temperatures than oxide ion conductors [4, 5]. Development of proton conducting ceramics started with Iwahara's reports on $SrCeO_3$ with proton conduction in 1981 [6], followed by $SrZrO_3$, $BaCeO_3$ and $BaZrO_3$ in 1983 [7]. More recently new proton conductors have been discovered, such as lanthanum tungstate in 2001 [8] and Ca-doped $LaNbO_4$ in 2006 [9]. The structural and chemical parameters determining formation and mobility of proton defects by formation of a solid solution of $Y:BaZrO_3$-$BaCeO_3$ system was discussed in a review in 2003 [10], resulting in a renewed interest in $BaZr_{1-x-y}Ce_xY_yO_3$ as a chemically stable, high temperature proton conductor. Figure 1-1 presents different proton conducting ceramics and their proton conductivities.
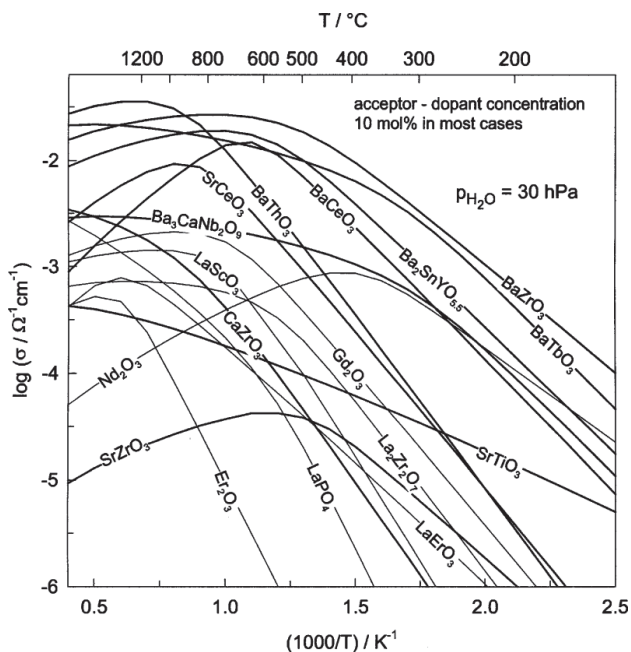
Figure 1-1: Examples of different proton conducting oxides and their conductivities [10].

Besides reaching sufficient electrolyte conductivity at intermediate temperatures, the most important challenge has, for both SOFC and PCFC, been the slow reaction kinetics at the cathode. The search for new mixed oxide ionic / electronic conductors (O-MIECs) with the required properties to serve as a cathode is one of the main focuses in developing high efficiency SOFCs / PCFCs. The most efficient cathode materials for SOFCs so far are Co-based perovskites such as $Sm_{0.5}Sr_{0.5}CoO_3$ (SSC) [11], $Ba_{0.5}Sr_{0.5}Co_{0.8}Fe_{0.2}O_{3-\delta}$ (BSCF) [12] and $La_{0.6}Sr_{0.4}Co_{0.2}Fe_{0.8}O_{3-\delta}$ (LSCF) [13, 14]. Unfortunately, these materials either show too high polarization resistances at intermediate temperatures or they are not chemically stable under operating conditions. Recently, high ionic and electronic conductivity have been reported at relatively low temperatures for B-site Co-based perovskites by substituting Rare Earth (RE) elements such as Pr and Gd for Ba on the A-sites. This results in layered double perovskites with alternating RE / Ba(Sr) layers where oxygen vacancies order in the RE layers, creating channels for oxide ion

transport [15]. The mixed conductivity of these double layered perovskites, e.g. $PrBa_{0.5}Sr_{0.5}Co_{0.8}Fe_{0.2}O_{5+\delta}$ [16], $GdBa_{1-x}Sr_xCo_2O_{5+\delta}$ [15] and the family of $LnBaCo_2O_{5+\delta}$ (Ln = La, Pr, Nd, Sm and Gd) [17] makes them promising materials for SOFC cathode candidates.

There is an increased interest in testing the best SOFC cathode materials for PCFCs, and several studies have presented promising results. In 2008, a PCFC with a 65 µm $BaZr_{0.1}Ce_{0.7}Y_{0.2}O_{3-\delta}$ (BZCY17) electrolyte and a $Sm_{0.5}Sr_{0.5}CoO_{3-\delta}$ (SSC) cathode was reported to reach a peak power density of 0.6 Wcm^{-2} at 650°C [18]. The same SSC cathode material was tested for SOFC application on a 25 µm electrolyte of $Sm_{0.2}Ce_{0.8}O_{1.9}$ [11]. Even though direct comparison is difficult, this interestingly gave a cell with lower peak power density at 500°C than the aforementioned PCFC at the same temperature, despite having less than half the electrolyte thickness. Another similar comparison that can be made is for BSCF tested as a cathode for both SOFC and PCFC applications. Shao and Haile [12] reported in their letter to Nature in 2004 a peak power density of 0.4 Wcm^{-2} at 500°C for an SOFC with a 20 µm electrolyte of $Sm_{0.15}Ce_{0.85}O_2$ and with a BSCF cathode. This is probably the best intermediate temperature SOFC performance reported so far. The same cathode material was tested on a 50 µm BCY electrolyte for PCFC applications [19]. In this study, a peak power density of 0.225 Wcm^{-2} was reported at 500°C. The SOFC power output was less than double that for PCFC, indicating that the PCFC can be capable of producing power densities in the range of the best reported SOFC. It is important to recognize the issues of stability and lifetime for both BCY and BSCF when applied as cell components.

In a more recent study [20], a similar BSCF cathode was tested on a 10-15 µm proton-conducting BZCY26 electrolyte. Peak power density was measured to slightly above 0.5 Wcm^{-2} at 600°C, and by testing the single cell reversibility, the ASR was measured to 0.46 and 0.26 Ωcm^2 for fuel cell and electrolysis modes, respectively (Figure 1-2). The BSCF electrode showed the ability to oxidize H_2O forming O_2 and protons, yielding a hydrogen evolution rate of 7.1 ml min^{-1} cm^{-2} at the cathode with a

current density of 1.5 Acm^{-2}, close to the theoretical faradaic production rate of 7.3 ml min^{-1} cm^{-2}.
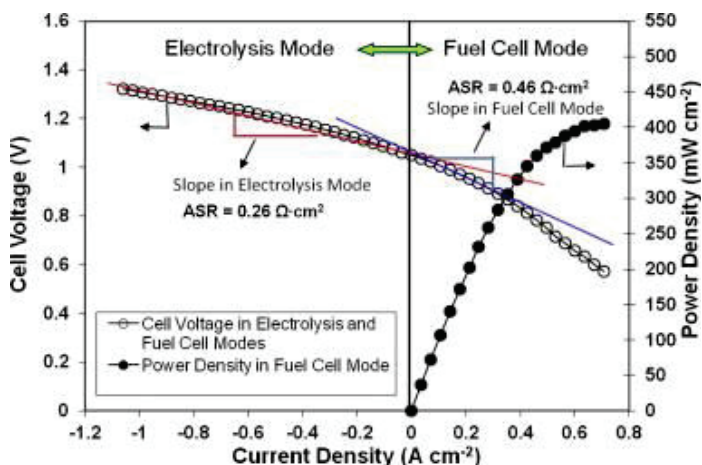
Figure 1-2: Performance of BZCY-based single cell in fuel cell and electrolysis mode at 600°C [20].

The latter results are intriguing in the sense that they open for new questions regarding the reaction mechanisms taking place at the oxygen electrode in both anodic and cathodic operation. The fact that oxidation of water seems to take place on BSCF in anodic operation, and given the high oxygen understoichiometry of 3-δ = ~2.3 at 600°C [21], investigations of the hydration properties and partial proton conductivity of BSCF and other O-MIEC perovskites is called for. Although the number of detailed studies of reaction kinetics for proton conducting oxygen-side electrodes is limited, it is widely accepted that a mixed protonic / electronic conductor (P-MIEC) as oxygen electrode would extend the triple phase boundary reaction $O + 2e^- + 2H^+ \leftrightarrow H_2O$ over the electrode surface [22, 23]. This is shown schematically in the illustration by Dailly et al. (Figure 1-3), who investigated the relation between hydration and electrode performance for Ln_2MO_4 based materials and perovskite BSCF. $Pr_2NiO_{4+\delta}$ and BSCF exhibit the best electrode performance, but there was no direct sign of significant hydration of the bulk. The $Ln_2MO_{4+\delta}$ materials have also been tested as SOFC cathodes, again with $Pr_2NiO_{4+\delta}$ as the best material [24].

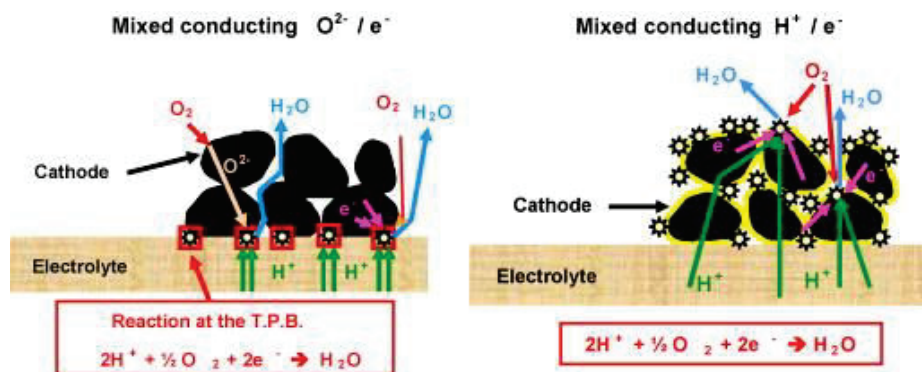*Figure 1-3: Illustration of difference between mixed proton / electronic and oxide ion / electronic conducting materials on air-side oxygen reaction by Dailly et al [22].*

In a more recent study, hydration and PCFC cathode performance of BSCF, $BaPrCo_2O_{5+\delta}$ (BPC), Pr_2NiO_4 (PNO) and LSCF [25] were studied. Under wet conditions at 600°C, the two first candidates showed highest water content whereas the two latter did not exhibit any significant uptake of water. Still, analysis of polarization resistances (R_p) showed enhanced performance for BSCF, BPC and PNO with increasing pH$_2$O. These three materials are in the paper referred to as "triple conducting oxides" showing conduction of electron holes, oxide ions and protons. Based on pO$_2$ and pH$_2$O dependencies of R_p, at 600°C it was concluded that the overall cathode reaction for the materials was rate limited by electrolyte / electrode interfacial proton transfer (PNO) and electrode water formation (BSCF, BPC, PNO). LSCF, which showed no hydration, displayed a negative dependency of R_p on pH$_2$O suggesting that ambient water inhibits the oxygen reduction reaction rather than being a reactant in cathodic operation. BPC and PNO showed the lowest R_p of the four.

1.2 Objectives

The first manuscript gives an overview of the status in Norway with respect to research and manufacturing of proton ceramic fuel cells at the end of 2009. In this manuscript, all PCFC parts are assessed in general. The main part of the PCFC research in Norway was up until then focused around the acceptor doped LaNbO$_4$ electrolyte, and fundamental PCFC cathode studies was in its infancy, not only in

Norway, but also in general. The 2009 state-of-the-art materials is the starting point for our studies.

The objectives of this work are

i.   To study the effect of ambient water on the operation of the oxygen electrode. Some studies have aimed to resolve the elementary cathodic reaction steps for PCFCs [25, 26]. The different systems show different properties, and all in all there is a need to know more about both the elementary reaction steps and how materials properties can be designed to optimize the performance of the PCFC oxygen electrode. The reversibility of the electrode, meaning whether it is capable of oxidizing water, is also of key importance, as hydrogen production from electrolysis is an upcoming technology in fields like energy storage for renewable energy systems.

ii. To investigate the effect of different microstructural improvements on the oxygen electrode performance. It has previously been shown that by microstructural processing, such as infiltration of the electronic phase on a backbone of the proton conducting electrolyte phase, a significant lowering of cathode ASR can be achieved [27]. Improvements of the tpb surface kinetics and micro structure by addition of nano-sized catalysts is a way to widen the tpb reaction zone and increase the reaction rate. Furthermore, fine-grained functional layers and graded porosity will give increased numbers of tpb reaction sites.

iii. To describe the electrode reactions in a system with more than one type of charge carriers. Most ionic electrolyte materials exhibit, to some extent, parallel transport of oxide ions and protons, the first normally dominating at high temperature, and the latter at low. In a transition temperature region, there will be mixed proton and oxide ion conductivity. A model will be developed, allowing R_p to be resolved in elementary reaction steps for protons and oxide ions, and the model

parameters will be fitted to the measured results, assigning partial resistances to each charge carrier and their individual rate limiting electrode process.

iv. To investigate cathode reactions under experimental conditions where oxide ions dominate the charge transport.

v. The investigations will show to what extent electrolyte transport of electron holes affect the measured polarization resistance. Studying electrode reactions at elevated temperatures in oxidizing conditions often entails increased partial electronic conductivity in the electrolyte material. This electronic conductivity will partially short circuit the cell. In an operating fuel cell or electrolyzer cell, the reducing conditions on the fuel side will create a barrier for *p*-type conductivity in the electrolyte and such a partial short circuit will therefore be less significant or non-existing. If the polarization resistance under operating conditions is to be investigated at high temperatures and under oxidizing conditions by separate electrode measurements, the electronic partial short circuit must be accounted for. The model in iii, separately accounting for different charge carriers will be elaborated to comprise also electron holes.

vi. To present new and improved PCFC cathode materials. Mixed conducting double perovskite materials with the general formula $BaRE_{1-x}La_xCo_{2-y}Fe_yO_{6-\delta}$ (RE = Gd, Pr) will be investigated as oxygen electrodes on a proton conducting electrolyte.

2. **Methodology**

Electrode measurements were performed by impedance spectroscopy on ceramic electrolyte supported button cells (discs) mounted in a ProboStat measuring cell (NorECs, Norway) as illustrated in Figure 2-1 [28]

Figure 2-1: Example of connection to disk samples for impedance measurements. The schematics show principle of spring loads and regular 2-electrode 4-wire setup with dual gas supplies and thermocouple [28].

The ProboStat is supplied with electrode and thermocouple feedthroughs as well as gas in- and outlets for both inner and outer compartments. By this, the sample environment can be controlled with respect to temperature and partial pressures of the reactant gasses. Figure 2-2 shows the base unit [28].

Inner chamber gas in
Inner chamber electrode and thermocouple contacts
Inner chamber gas out
Outter chamber gas in
Sample support tube threads & o-ring
Outter chamber gas out
Electrode and thermocouple feedthroughs
Water cooling (or heating) in and out
Thermocouple contacts
BNC contacts
Quick connects for gases
BNC contacts
Switches for shields etc. not visible here

Figure 2-2: ProboStat base unit with feedthroughs [28].

The various gas mixtures were obtained by use of an in-house built gas mixer designed to control the dilution of reactant gasses as well as the water vapor pressure in the measurement cell. A schematic illustration of the gas mixer is given in Figure 2-3.
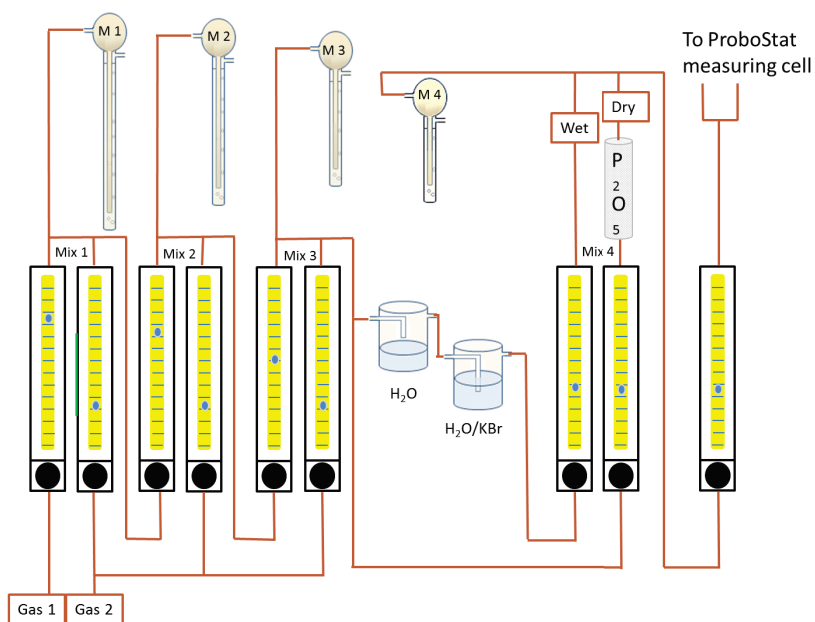
Figure 2-3: Schematic illustration of gas mixer.

The electrodes were applied to the pellets in several ways, as described separately in each manuscript. Impedance measurements were performed in two-point and three-point configurations, where two wires (current lead and voltage probe) were contacted to the top (working) electrode and the bottom electrode acted as counter electrode contacted by the low current lead. The low potential probe was contacted to the counter electrode in the two point configuration, and to a reference electrode painted around the pellet circumference in the three point configuration. Figure 2-4 illustrates the three point configuration.
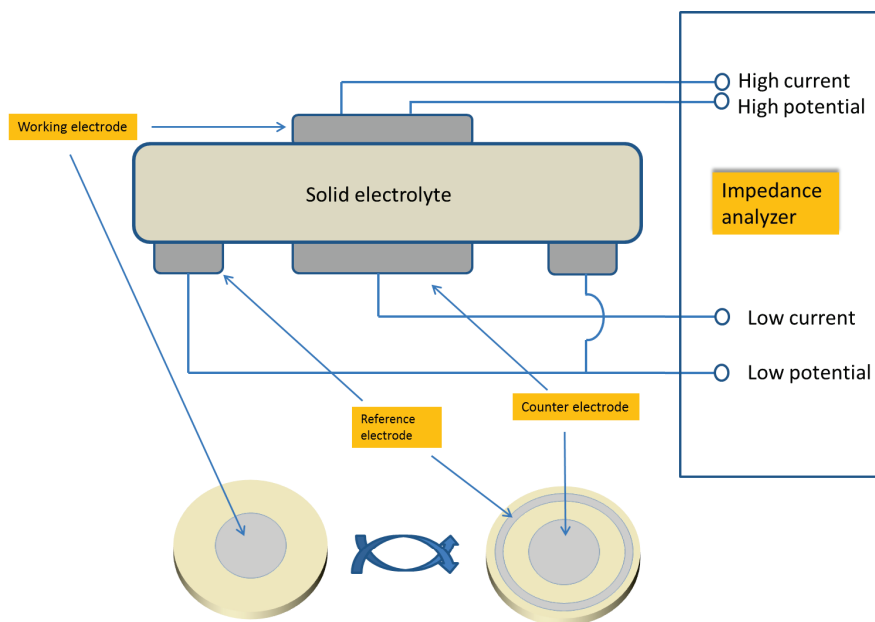
Figure 2-4: Three point configuration with working, counter and reference electrodes connected to the impedance analyzer.

The Impedance measurements were conducted with oscillating voltages between 15 and 50 mV RMS in the frequency range 1 MHz to 1 µHz. Different temperatures and gas environments demand different voltages and frequency ranges, and for high electrode impedances with slow relaxation, it turned out to be necessary to measure down to as low frequencies as 1 µHz. The voltage amplitude was set as low as possible to avoid affecting the activation energy of the electrode reaction by the applied voltage and also to avoid diffusion controlled conditions for the charge transfer current. The impedance data were deconvoluted by use of the ZView software from Scribner Associates, Inc.

3. **Theory**

3.1 Proton ceramic fuel cells

The PCFC is characterized by oxidation of H_2 at the anode, transport of protons in the dense ceramic electrolyte, reduction of oxygen at the cathode and transfer of protons across the electrolyte / cathode interface to produce water at the oxygen side, as illustrated in Figure 3-1.
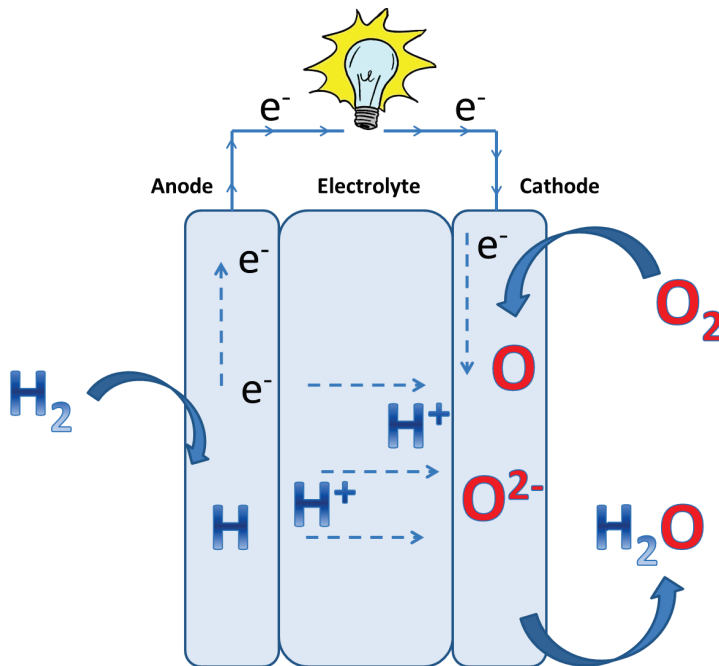
Figure 3-1: Illustration of a proton ceramic fuel cell (PCFC).

The ideal ceramic electrolyte is a pure proton conductor. In such a proton conductor, the conductivity is expressed by the concentration and mobility of the protons. There are, however, often more charge carriers contributing to the overall conductivity. Seeing these charge carriers as defects in the perfect metal oxide structure enables the quantification of partial conductivities.

3.1.1 Defects

Some metal oxides dissolve hydrogen in the form of protons in their oxygen sublattice, creating hydroxide groups on oxygen sites (OH_O^-) [29]. The dissolution of protons into the electrolyte of a running PCFC happens at the hydrogen anode:

$$H_2(g) + 2O_O^{2-}(\text{electrolyte}) \leftrightarrow 2OH^-(\text{electrolyte}) + 2e^-(\text{electrode}) \tag{1}$$
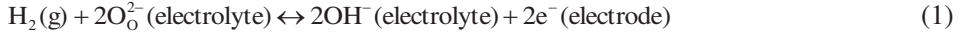
The proton concentration in the PCFC electrolyte can be increased by acceptor doping the electrolyte material. This is done by introducing a foreign metal of for example one less positive charge than the native metal, forming monovalent, effectively negative acceptor sites ($Mf_M^/$). The acceptors are charge compensated in the structure by the formation of oxygen vacancies, $v_O^{\bullet\bullet}$ which can be hydrated by dissolution of more proton defects.

Oxygen vacancies can be formed also intrinsically, by Schottky disorder or oxygen deficit at external and internal surfaces, charge compensated by metal vacancies or electrons. Or they can form in intrinsic Frenkel reactions inside the material, where lattice oxide ions are in equilibrium with oxygen vacancies and interstitials. Equation 2 is an example of formation of oxygen vacancies and electrons.

$$O_O^x \leftrightarrow v_O^{\bullet\bullet} + 2e^/ + 1/2O_2(g) \tag{2}$$

By introducing acceptor dopants, the oxygen vacancy concentration is increased and fixed, and under the relevant temperature and atmospheric conditions, concentrations of acceptors and vacancies (in dry state) and / or protons (in hydrated state) will be much higher than that of electronic defects in a typical electrolyte material. The dissolution of MO in a M_2O_3 metal oxide can be written

$$2MfO(s) \rightarrow 2Mf_M^/ + v_O^{\bullet\bullet} + 2O_O^x \tag{3}$$

The electroneutrality in the dry state, dominated by acceptors and oxygen vacancies, can then be approximated by:

$$2\left[v_O^{\bullet\bullet}\right] = \left[Mf_M^{/}\right] = \text{constant} \tag{4}$$

In an ionic conductor (oxide ion or proton conducting), electronic defects (electrons and electron holes) are present in small concentrations contributing to minor n- and p-type conductivities. These minority defects are formed by intrinsic thermal excitation across the semiconductor band gap or as charge compensators when temperature or pressure conditions cause the material to deviate from stoichiometry. One example of this, formation of oxygen vacancies charge compensated by electrons is given in Equation 2. An equilibrium constant for the formation of electrons in the dry state (K_n) as given in Equation 2 can be written

$$K_n = \frac{\left[v_O^{\bullet\bullet}\right]}{\left[O_O^x\right]} n^2 pO_2^{1/2} \tag{5}$$

Under extrinsic conditions, dominated by acceptors and oxygen vacancies, the combination of Equations 4 and 5 gives the concentration of minority electrons, expressed by the equilibrium constant for reaction 2, the acceptor dopant concentration, and pO_2:

$$n = (2K_n)^{1/2}\left[Mf_M^{/}\right]^{-1/2} pO_2^{-1/4} \tag{6}$$

The oxidation of oxygen vacancies to create electron holes can be written

$$1/2O_2(g) + v_O^{\bullet\bullet} \leftrightarrow O_O^x + 2h^{\bullet} \tag{7}$$

By using the equilibrium constant for the formation of electron holes in dry state (K_p), a pO_2-dependency for the concentration of electron holes can be obtained

$$p = (2K_p)^{1/2}\left[Mf_M^{/}\right]^{1/2} pO_2^{1/4} \tag{8}$$

The oxygen vacancies can be hydrated in wet atmospheres given favorable hydration thermodynamics. The hydration of oxygen vacancies can be written

$$H_2O(g) + v_O^{\bullet\bullet} + O_O^x \leftrightarrow 2OH_O^{\bullet} \tag{9}$$

The formation of electrons in hydrated state can be given by combining Equations 2 and 9.

$$H_2O(g) + 2O_O^x \leftrightarrow 2OH_O^\bullet + 2e' + 1/2 O_2(g) \tag{10}$$

The formation of electron holes comes in the same way by the combination of Equations 7 and 9.

$$2OH_O^\bullet + 1/2 O_2(g) \leftrightarrow 2O_O^x + 2h^\bullet + H_2O(g) \tag{11}$$

The simplified electroneutrality condition in the extrinsic region when all oxygen vacancies are hydrated is

$$[OH_O^\bullet] = [Mf_M'] = \text{constant} \tag{12}$$

Using the equilibrium constants for the formation of electrons and protons, the concentrations of electrons and holes can be given by

$$n = \left(K_n K_{Hydr}\right)^{1/2} [Mf_M']^{-1} pH_2O^{1/2} pO_2^{-1/4} \tag{13}$$

and

$$p = \left(K_p K_{Hydr}^{-1}\right)^{1/2} [Mf_M'] pH_2O^{-1/2} pO_2^{1/4} \tag{14}$$

The hydration equilibrium constant of reaction 9, is a function of the standard entropy and enthalpy of hydration (ΔS_{Hydr}^0 and ΔH_{Hydr}^0)

$$K_{Hydr} = \frac{[OH_O^\bullet]^2}{[O_O^x][v_O^{\bullet\bullet}]pH_2O} = \exp\left(\frac{\Delta S_{Hydr}^0}{R}\right)\exp\left(\frac{-\Delta H_{Hydr}^0}{RT}\right) \tag{15}$$

And the electroneutrality under extrinsic conditions, including both oxygen vacancies and protons is

$$2[v_O^{\bullet\bullet}] + [OH_O^\bullet] = [Mf_M'] = \text{constant} \tag{16}$$

When the defect concentrations are relatively small, and the concentration of oxygen on oxygen sites can be considered equal to the stoichiometric composition, the concentration of protons is given by a standard concentration expression derived from the hydration equilibrium expression (Equation 15) and the electroneutrality for protons, oxygen vacancies and dopants (Equation 16):

$$[OH_o^{\bullet}] = \frac{[O]K_{Hydr}pH_2O\left(-1+\sqrt{1+\frac{8[Mf_M']}{[O]\,K_{Hydr}pH_2O}}\right)}{4} \tag{17}$$

The combination of Equations 16 and 17 gives correspondingly the concentration of oxygen vacancies.

$$[v_O^{\bullet\bullet}] = \frac{1}{2}\left([Mf_M'] - \frac{[O]K_{Hydr}pH_2O\left(-1+\sqrt{1+\frac{8[Mf_M']}{[O]\,K_{Hydr}pH_2O}}\right)}{4}\right) \tag{18}$$

The pO_2 and pH_2O dependencies of electrons and holes can be found by combining the expression for the concentration of protons (Equation (17)) and the red-ox equilibria in wet conditions (reactions in Equations 10 and 11).

$$n = (K_n K_{Hydr})^{1/2}pH_2O^{1/2}pO_2^{-1/4}\left(\frac{[O]K_{Hydr}pH_2O\left(-1+\sqrt{1+\frac{8[Mf_M']}{[O]\,K_{Hydr}pH_2O}}\right)}{4}\right)^{-1} \tag{19}$$

$$p = (K_p K_{Hydr}^{-1})^{1/2}pH_2O^{-1/2}pO_2^{1/4}\left(\frac{[O]K_{Hydr}pH_2O\left(-1+\sqrt{1+\frac{8[Mf_M']}{[O]\,K_{Hydr}pH_2O}}\right)}{4}\right) \tag{20}$$

Schematic variations of all charge carrying defects in the extrinsic region as a function of pO_2 and pH_2O are given in Figures 3-2 and 3-3, respectively.
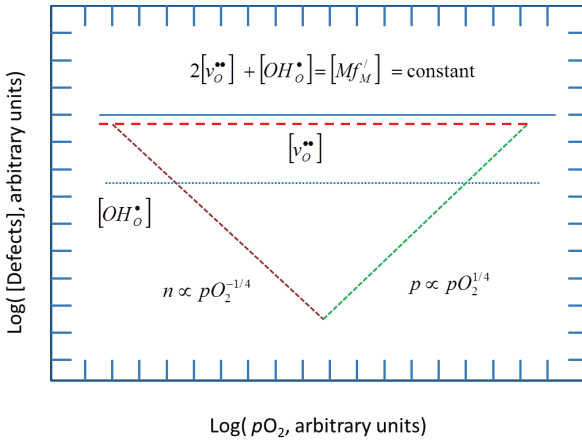
Figure 3-2: Concentrations of oxygen vacancies, protons and electronic defects as a function of pO2 when the oxygen vacancy concentration dominates over protons, determined by the concentration of acceptor dopants.
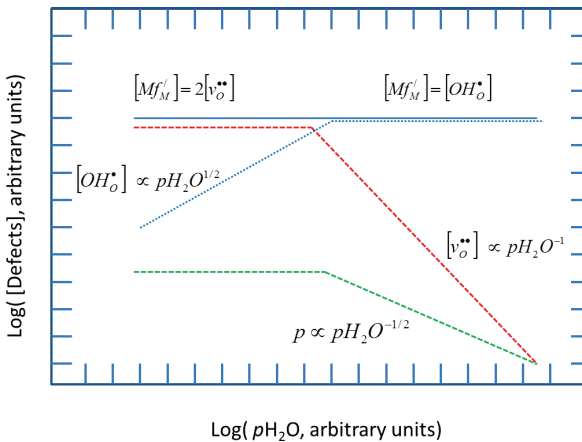
Figure 3-3: Concentrations of protons, oxygen vacancies and electron holes as a function of water vapor pressure under oxidizing conditions in a material where the acceptor dopants are charge compensated by oxygen vacancies or protons, depending on pH2O.

3.1.2 Transport

The conductivity, σ_i, of a charged species, i, is given by its charge, $z_i e$, its concentration, c_i and its mobility, μ_i.

$$\sigma_i = z_i e c_i \mu_i \tag{21}$$

The total electrolyte conductivity in oxidizing conditions is $\sigma_{tot} = \sigma_{H^+} + \sigma_{v_O^{\bullet\bullet}} + \sigma_h$. The partial conductivities, σ_i, may change relative to each other when changing measurement or operation conditions. The charge carrier concentrations are described above. The concentration term favours proton transport at lower temperatures, and though the concentration of protons decreases with increasing temperature, proton conductivity goes through a maximum due to the higher mobility at higher temperatures. The mobility of a diffusing charged species, i, in the case of ions and charged point defects as well as small polaron electronic defects can be written

$$\mu_i = \mu_i^0 \frac{1}{T} \exp\left(\frac{-\Delta H_{mob,i}}{RT} \right) \tag{22}$$

The proton conductivity is hence expressed as

$$\sigma_{H^+} = \mu_{H^+} c_{H^+} z_{H^+} e = F\left[OH_O^{\bullet}\right] d_m \mu_{H^+}^0 \frac{1}{T} \exp\left(\frac{-\Delta H_{mob,H^+}}{RT} \right) \tag{23}$$

Here, z_{H^+} is 1 and d_m is the molar density of the material. Protons move in the oxide through jumps between adjacent oxide ions, where ΔH_{mob} is the enthalpy associated with the jump. This mechanism is termed the "Grotthuss mechanism", and the pre-exponential factor can be expressed [30]

$$\mu_{H^+}^0 = \frac{Z\lambda^2 e^2 v^0}{6Vk_B} \tag{24}$$

, where Z is the number of jump directions, λ is the jump distance (O-O distance), e is the elementary charge, v^0 is the attempt frequency, V is the unit cell volume and k_B is the Boltzmann constant.

At higher temperatures, mobile oxygen vacancies in the electrolyte will facilitate a partial net transport of oxide ions. Combining Equations 16, 21 and 22, the partial oxide ion conductivity can be written

$$\sigma_{v_O^{\bullet\bullet}} = \mu_{v_O^{\bullet\bullet}} c_{v_O^{\bullet\bullet}} z_{v_O^{\bullet\bullet}} e = F\left(\left[Mf_M^{/}\right] - \left[OH_O^{\bullet}\right]\right) d_m \frac{1}{T} \mu_{v_O^{\bullet\bullet}}^0 \exp\left(\frac{-\Delta H_{mob,v_O^{\bullet\bullet}}}{RT}\right)$$

(25)

The proton and oxide ion conductivities can be obtained from Eqs. 23 and 25, respectively, after insertion of simplified or full expressions for the proton concentrations from the preceding section.

The mobilities of electrons and holes are much higher than the mobilities of protons and oxygen vacancies. Therefore, these minority defects often contribute to the total conductivities at higher temperatures and under reducing (electrons) or oxidizing (holes) conditions. At high temperatures, electronic defects are more often localized at metal sites, and the transport mechanism is regarded as a jumping process (small polaron hopping). Combining Equations 21 and 22 gives an expression for p-type conductivity

$$\sigma_h = Fpd_m\mu_h^0 \frac{1}{T}\exp\left(\frac{-\Delta H_{mob,h^{\bullet}}}{RT}\right)$$

(26)

Inserting Equation 8 and 20 for the electron hole concentration, p, will give partial p-type conductivity with pressure dependencies in dry and wet conditions, respectively.

In the characterization of fuel cell components, and electrodes in particular, it is important to bring the contributions from the various charge carriers to the electrolyte conductivity under control. If the electrolyte exhibits a mix between two or more charge carriers, the reactions at the electrodes will be affected accordingly.

3.2 Red-ox potential

Electrode reactions most often occur across a phase boundary. In solid state electrochemistry, reactions take place not only over the electrode / electrolyte phase

boundary, but also at the interface between the electrode and the gas phase. The reduction of an adsorbed hydroxyl by the transfer of one electron at a metal electrode is an example:

$$e^-(\text{metal}) + OH(\text{electrode surface}) \leftrightarrow OH^-(\text{electrode surface}) \tag{27}$$

The difference in potential of the electron in the metal (the Fermi level) and in the available orbital of the hydroxyl molecule constitutes a driving force towards equilibrium where difference in chemical potentials, $\Delta\mu$, is balanced against difference in electric potential, $\Delta\varphi$. The sum of these two potentials is called the difference in electrochemical potential, $\Delta\tilde{\mu}$.

$$\Delta\tilde{\mu}_i = \Delta\mu_i + zF\Delta\varphi \tag{28}$$

If adsorbed hydroxyls are considered to be in equilibrium with the surrounding oxygen gas and water vapor, the chemical potential of adsorbed OH can be written:

$$4\mu_{OH(ads)} = \mu_{O_2(g)} + 2\mu_{H_2O(g)} \tag{29}$$

The chemical potential of a reactant, i, is related to its activity through

$$\mu_i = \mu_i^0 + RT\ln(a_i) \tag{30}$$

One can thus write for oxygen gas

$$\mu_{O_2(g)} = \mu_{O_2(g)}^0 + RT\ln\left(\frac{pO_2}{pO_2^0}\right) \tag{31}$$

and for water vapor:

$$\mu_{H_2O(g)} = \mu_{H_2O(g)}^0 + RT\ln\left(\frac{pH_2O}{pH_2O^0}\right) \tag{32}$$

For the transfer of one electron between electrode interior and the adsorbed hydroxyl, we have for the change in electrochemical potential:

$$\Delta\tilde{\mu} = \tilde{\mu}_{OH^-(ads)} - \mu_{OH(ads)} - \tilde{\mu}_{e^-(metal)} \tag{33}$$

By inserting Equation 29 in Equation 33, the electrochemical potential change is

$$\Delta\tilde{\mu} = \tilde{\mu}_{OH^-(ads)} - \frac{\mu_{O_2(g)}}{4} - \frac{\mu_{H_2O(g)}}{2} - \tilde{\mu}_{e^-(metal)} \tag{34}$$

Equilibrium is reached when $\Delta\tilde{\mu} = 0$, and hence:

$$\frac{\mu_{O_2(g)}}{4} + \frac{\mu_{H_2O(g)}}{2} + \tilde{\mu}_{e^-(metal)} = \tilde{\mu}_{OH^-(ads)} \tag{35}$$

If we now want to relate the equilibrium potential to pO_2 and pH_2O, we insert Equations 31 and 32:

$$\frac{\left(\mu^0_{O_2(g)}\right)}{4} + \frac{RT}{4}\ln(pO_2) + \frac{\left(\mu^0_{H_2O(g)}\right)}{2} + \frac{RT}{2}\ln(pH_2O) + \tilde{\mu}_{e^-(metal)} = \tilde{\mu}_{OH^-(ads)} \tag{36}$$

, which can be simplified to

$$\frac{\left(\mu^0_{O_2(g)}\right)}{4} + \frac{\left(\mu^0_{H_2O(g)}\right)}{2} + RT\ln\left(pO_2^{\frac{1}{4}}pH_2O^{\frac{1}{2}}\right) + \tilde{\mu}_{e^-(metal)} = \tilde{\mu}_{OH^-(ads)} \tag{37}$$

To separate the chemical and electrical potentials, we use the relation given in Equation 28 and get

$$\frac{\left(\mu^0_{O_2(g)}\right)}{4} + \frac{\left(\mu^0_{H_2O(g)}\right)}{2} + RT\ln\left(pO_2^{\frac{1}{4}}pH_2O^{\frac{1}{2}}\right) + \mu^0_{e^-(metal)} - F\varphi_{(metal)} = \mu^0_{OH^-(ads)} - F\varphi_{(OH^-)} \tag{38}$$

Here, $\varphi_{(OH^-)}$ is the electric potential felt by the electron in the OH orbital most likely to be occupied. The difference in electric potential is thus

$$\left(\varphi_{(metal)} - \varphi_{(OH^-)}\right) = \frac{\left(\mu^0_{O_2(g)}\right)}{4F} + \frac{\left(\mu^0_{H_2O(g)}\right)}{2F} + \frac{\mu^0_{e^-(metal)}}{F} - \frac{\mu^0_{OH^-(ads)}}{F} + \frac{RT}{4F}\ln\left(pO_2 \, pH_2O^2\right) \tag{39}$$

, or

$$\Delta \varphi = \Delta \varphi^0 + \frac{RT}{4F} \ln\left(pO_2 pH_2O^2\right) \tag{40}$$

, where $\Delta \varphi^0$ is the standard half-cell potential. The electric potential, $\Delta \varphi$, is the potential difference for electrons in the electrode orbitals versus in the available orbitals of the adsorbed hydroxyls. Equation 40 yields the Nernst equation for the electrode half-cell reduction potential.

3.3 Reaction rate expressions

When elementary reaction steps take place between gas phase and surface, on the electrode surface, between electrode bulk and adsorbates, and between the electrode and the electrolyte, there are energy barriers to overcome. The electron orbitals in the metal electrode are prone to be extended somewhat beyond the outermost atomic layer at the surface as a result of kinetic energy. This extension can induce a dipole layer where adsorbed molecules, atoms or ions are oriented in one direction, causing electrostatic repulsions towards adsorption of reactants and transfer of charged species. The adsorption layer is charge compensated in the outermost electrode layers by accumulations or depletions of electrons and thereby changing the work function of the electrode [31]. The build-up and discharge of these surface dipole layers are seen as capacitive contributions to the electrochemical current, and will contribute to the polarization of the electrode. In addition there is a double-layer impedance with interfacial accumulations or depletions of charge carriers giving rise to capacitive current at the electrode / electrolyte interface.

For a current to pass, thermal or electrical energy must be supplied to overcome these barriers. This *activation energy* (E_A) can be determined by the temperature dependency of the electron transfer rate (Figure 3-4).
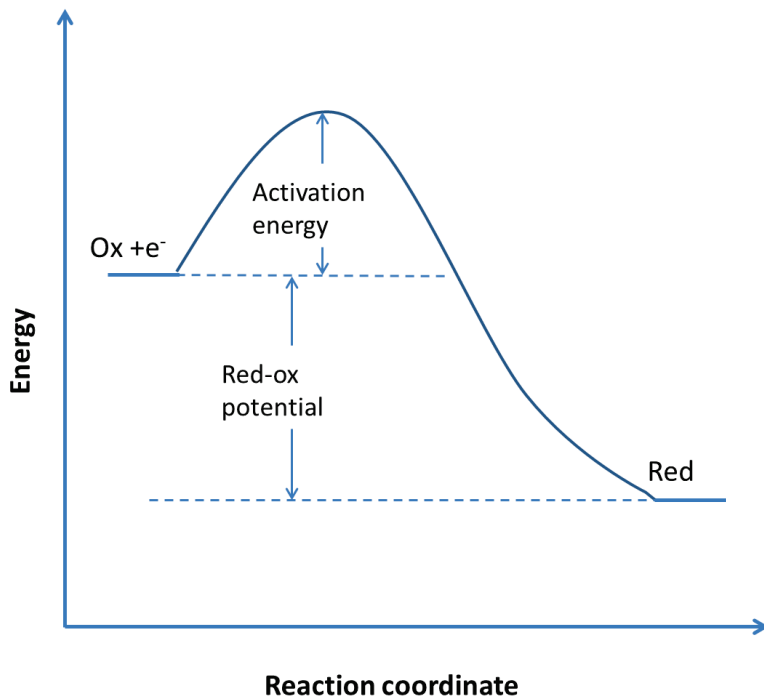
Figure 3-4: Energy diagram of electron transfer in a red-ox process.

When studying electrode reactions, as the one in Equation 27, we are interested in current vs voltage relations. The current is proportional to the reaction rate through Faraday's law, and the potential loss when a current is running determines the resistance of the investigated process over which the potential drop is measured. Therefore, we seek to describe the reactions by their rates at given applied potentials and partial pressures

$$r = a_{ox}^{x} k^{+} \exp\left(-\frac{nFE}{RT}\right) - a_{red}^{y} k^{-} \exp\left(\frac{nFE}{RT}\right) \tag{41}$$

Here, the reaction is seen in forward direction upon reduction in cathodic operation, k^{+} and k^{-} are rate constants in the forward and backward direction and n is number of electrons in the reaction. Since the chemical potentials are dependent on concentration, a concentration term, a, with reaction orders x and y for oxidized and

reduced species, respectively, is incorporated in the rate expression. As the surface coverage of one species is dependent on available adsorption sites and partial pressure of the adsorbing gas, it can sometimes also be useful to relate the surface coverage, and thus also the rate of the electrochemical reaction, to partial pressures of other adsorbing gasses that might affect the availability of adsorption sites. Most often, however, surface coverage dependencies of reaction rates are given at low surface coverages, where adsorption sites are abundant and competing absorbents are neglected.

As seen earlier, $\Delta\varphi$ is the difference in electrical potential for the electrons in the electrode material versus in the available orbital of the oxidized adsorbate. Converted to energy, we thus have

$$E_F - E_{Ox}^0 = ne\Delta\varphi = neE_{red} \tag{42}$$

, where e is the electron charge and E_{Ox}^0 is the average energy of the adsorbate orbitals most likely to be occupied by the transferred electrons. Furthermore, an applied potential, η, alters the potential of the metal by shifting its Fermi energy level, E_F, relative to E_{Ox}^0:

$$E_F(\eta) - E_{Ox}^0 = ne_0E_{red} + ne_0\eta \tag{43}$$

The rate expression in Equation 41 can thus be written as

$$r = a_{ox}^{m,n}k^+ \exp\left(-\frac{nF(E_{red}+\eta)}{RT}\right) - a_{red}^{m,n}k^- \exp\left(\frac{nF(E_{red}+\eta)}{RT}\right) \tag{44}$$

By inserting Equation 40 for E_{red}, the pO_2- and pH_2O-dependency of the half-cell potential can be merged with any possible concentration related pO_2- or pH_2O-dependency given by $a_{ox}^{m,n}$ and $a_{red}^{m,n}$. In this way, the partial pressure dependencies of the measured resistance can be compared with the theoretical dependencies of the reaction rate. If we simplify Equation 44 and multiply with F and the area, A, we have an expression for the electrochemical current density, i, which is a form of the Butler-

Volmer equation. By convention, forward direction is now anodic operation. The pO_2- and pH_2O-dependencies are incorporated in the exchange current density, i_0.

$$i = A \, i_0 \exp\left[\left(\frac{\alpha n F \eta}{RT}\right) - \exp\left(-\frac{\beta n F \eta}{RT}\right)\right] \tag{45}$$

Here, α and β are coefficients related to the symmetry of the energy barrier in anodic and cathodic direction, respectively. For a one-electron process, $\alpha + \beta = 1$.

The rate expression (Equation 44) can be used also for other elementary electrode steps than the electron transfer in Equation 27, making it possible to relate current, potential and measured partial electrode resistances to partial pressures of the reactant gasses.

3.4 Electrochemical processes at the oxygen electrode

The electrochemical red-ox reaction at the oxygen electrode is a multistep process, in which several species can be involved, and where the rates of each reaction step is dependent on the physical properties of the electrode materials as well as on the concentrations of, interactions between and mobilities of the involved species. Normally these processes are divided into two sub-groups; one involving all types of adsorption, desorption and diffusion of reactants and products, both in gas phase, on surfaces and in electrode interior, and another one describing processes of exchanging charge across different interfaces. These two divisions of processes will from now on be abbreviated d (diffusion) and ct (charge transfer).

In a PCFC, water is formed on the cathode side, and hence there will be ambient H_2O in the vicinity of the triple phase boundary (tpb). There are several interaction possibilities between the electrode surface, electrolyte surface, H_2O and O_2.

The overall reaction in the PCFC oxygen electrode is:

$$O_2(g) + 4H^+ + 4e^- \leftrightarrow 2H_2O(g) \tag{46}$$

This can be divided into a series of elementary reaction steps, first presented by Uchida, Tanaka and Iwahara in 1984 as a five-step process [32]. Later, the reaction series has been elaborated [26], suggesting a reaction series divided in eight steps (Table 3.4-1):

Table 3.4-1: PCFC elementary cathode reaction step series [26]

Reaction step	Elementary reaction	m	n
1	$O_2(g) \leftrightarrow 2O_{ads}$	1	0
2	$O_{ads} + e^- \leftrightarrow O_{ads}^-$	3/8	0
3	$O_{ads}^- \leftrightarrow O_{TPB}^-$	1/4	0
4	$O_{TPB}^- + e^- \leftrightarrow O_{TPB}^{2-}$	0	0
5	$OH_{electrolyte}^- \leftrightarrow H_{TPB}^+ + O_{electrolyte}^{2-}$	0	1/2
6	$O_{TPB}^{2-} + H_{TPB}^+ \leftrightarrow OH_{TPB}^-$	0	1/2
7	$OH_{TPB}^- + H_{TPB}^+ \leftrightarrow H_2O_{TPB}$	0	1
8	$H_2O_{TPB} \leftrightarrow H_2O(g)$	0	1

The columns m and n in Table 3.4-1 give the reaction orders, $R \propto pO_2^{-m} pH_2O^{-n}$ for the resistance associated with each elementary reaction step. These reaction orders are commonly used to assign polarization resistance to one or more of the suggested reaction steps. By doing so, it is important to bear in mind that these reaction orders are theoretical, valid at low surface coverages only and that real systems are affected also by other processes, such as electrostatic repulsions from adsorbed species [33] and competitive adsorption behaviour involving also other gaseous species. Still, the logarithmic pO_2-and pH_2O dependencies give valuable information regarding the nature of the rate limiting reaction step.

Table 3.4-1 presents a simplified reaction series, where step 3 describes the transport of O^- from the electrode surface to the TPB without further elucidation of the transport mechanism. In reality this transport can be facilitated in several ways. O can diffuse neutral, singly- or doubly charged, and even as hydroxyls or hydroxide ions on the electrode surface. It can also be transported in parallel to the surface diffusion as O^{2-} through electrode bulk and out at tpb if the electrode material is an O-MIEC.

An example of a more elaborated reaction path for a PCFC composite cathode has recently been suggested. In the study, it is reported that an oxide ion conductor such as $Ce_{0.8}Sm_{0.2}O_{2-\delta}$ (SDC) can cooperate with an electrocatalytic O-MIEC such as $Sm_{0.5}Sr_{0.5}CoO_3$ (SSC) to work as a composite cathode on a PCFC with a $BaCe_{0.8}Sm_{0.2}O_{3-\delta}$ (BCS) electrolyte, and that this composite improves cathode performance as compared to a composite electrode with a proton conductor as ionic component. To explain this unexpected phenomenon, a series of reaction steps is presented that involves the transfer of OH$^-$ across the electrolyte / electrode interface, moving from a regular O site in the proton conducting electrolyte, leaving an oxygen vacancy in the electrolyte and an interfacial surface hydroxide:

$$OH_O^- \leftrightarrow OH_{interf}^- + v_O \tag{47}$$

As there is fast oxide transport in the electrode material, the electrolyte vacancy is rapidly consumed and transferred to the electrode material by the transfer of one O^{2-} from the electrode to the electrolyte:

$$O_{O(cathode)}^{2-} + v_{O(electrolyte)} \leftrightarrow O_{O(electrolyte)}^{2-} + v_{O(cathode)} \tag{48}$$

a

H-TPB

SSC

BCS

$OH_o^•$

H-TPB at interface

Interface

$OH_o^•$ BCS

b

O-TPB

SSC

SDC

$O_o^×$

H-TPB at interface

Interface

$OH_o^•$ BCS
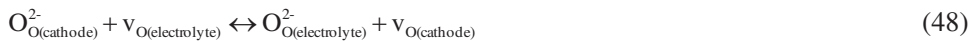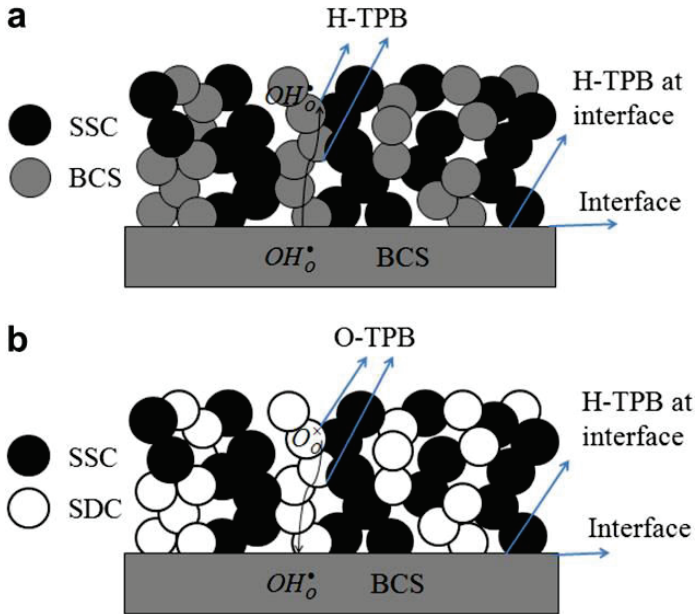
Figure 3-5: The schematic diagrams showing the different cathode reaction models of (a) SSC+BCS and (b) SSC+SDC. With SSC+BCS, oxygen is reduced and water is formed at the same sites (H-TPB). With SSC+SDC, oxygen is reduced at O-TPB while water is formed at interface site where proton and oxygen-ion are available. Oxygen reduction and water generation also occurs at H-TPB confined to the interface of SSC+SDC [34].

In this way, a net transfer of one proton has taken place, assisted by the oxide ion conducting electrode material [34]. The suggested reaction series is presented in Table 3.4-2.

Table 3.4-2: PCFC elementary cathode reaction series for an O-MIEC / oxide ion conductor composite electrode with pO_2 and pH_2O reaction orders m and n [34].

Reaction step	Elementary reaction	m	n
1.	$O_2(g) \leftrightarrow 2O_{ads}$	1	0
2.	$O_{ads} + e^- \leftrightarrow O_{ads}^-$	3/8	0
3.	$O_{ads}^- \leftrightarrow O_{TPB}^-$	1/4	0
4.	$O_{TPB}^- + e^- \leftrightarrow O_{TPB}^{2-}$	1/8	0
5.	$O_{TPB}^{2-} + v_{O(TPB)} \leftrightarrow O_{O(TPB)}^{2-}$	0	0
6.	$O_{TPB}^{2-} + v_{O(interf.cathode)} \leftrightarrow O_{O(interf.electrode)}^{2-} + v_{O(TPB)}$	0	0
7.	$OH_{O(bulk.electrolyte)}^- \leftrightarrow OH_{interf.electrolyte}^-$	0	1/2
8.	$OH_{O(interf.electrolyte)}^- \leftrightarrow OH_{interface}^- + v_{O(interf.electrolyte)}$	0	1/2
9.	$v_{O(interf.electrolyte)} + O_{O(interf.electrode)}^{2-} \leftrightarrow O_{O(electrolyte)}^{2-} + v_{O(electrode)}$	0	0
10.	$OH_{O(interf.electrolyte)}^- + OH_{interface}^- \leftrightarrow H_2O_{interface} + O_{O(interf.electrolyte)}^{2-}$	0	1
11.	$H_2O_{interface} \leftrightarrow H_2O(g)$	0	1

The reaction series in Table 3.4-2 is more elaborate than the series presented in Table 3.4-1, but nevertheless, it bears the same weaknesses regarding transport mechanisms and reactant interactions, even though Table 3.4-2 present a new perspective on the interfacial charge transfer reaction. The kinetic models in Tables 3.4-1 and 3.4-2 are, however, insufficient when an elementary reaction step has m and n both $\neq 0$, which can easily be the case, especially for surface reactions. It is also worth noting that while in Table 3.4-1 m for reaction step 4, electron transfer is reported to be 0. Table 3.4-2 claims it to be 1/8. This disagreement is not pursued here.

3.5 Impedance spectroscopy

3.5.1 Impedance

The electric double layer at the electrode / electrolyte interface contributes to the polarization, constituting a charge transfer resistance (R_{ct}) and a double layer

capacitance (C_{dl}). Surface exchange, accumulation of adsorbates and interaction between these causes polarization of the surface layers, and this polarization can, as a first approximation, be described as a parallel combination of a resistor and a plate capacitor [33]. The surface related capacitance and resistance will in this work be labelled "diffusion capacitance" (C_d) and "diffusion resistance" (R_d), respectively.

The accumulation and depletion of charge in the double layers at the surface and electrode / electrolyte interface exhibit discrete relaxation time constants, τ. When performing electrochemical impedance spectroscopy (EIS), a small AC perturbation with frequencies corresponding with τ gives a phase shift between current and potential, θ, and the complex relation between relaxation and phase shift is simplified through Fourier transforms of the current and voltage from the time to the frequency domain. By doing this, the AC current potential relation becomes similar to the Ohm's law DC relation.

$$Z(j\omega) = U(j\omega)/I(j\omega) \tag{49}$$

The impedance of the double layer is well represented by a parallel combination of a resistor and a capacitor, where $Z(\omega)$, is related to capacitance, C, and resistance, R, through

$$Z_{RC}(\omega) = \frac{R - j\omega R^2 C}{1 + \omega^2 R^2 C^2} \tag{50}$$

It can be seen from Equation 50 that at DC conditions, $Z_R(DC) = R$ and that a pure capacitive impedance (or reactance) is $Z_C(\omega) = 1/(j\omega C)$. Furthermore, $Z(\omega)$ can be expressed by its real and imaginary components:

$$Z(\omega) = Z' + jZ'' \tag{51}$$

And by plotting the impedance with polar coordinates, we can see the relation between impedance, |Z|, and phase angle:
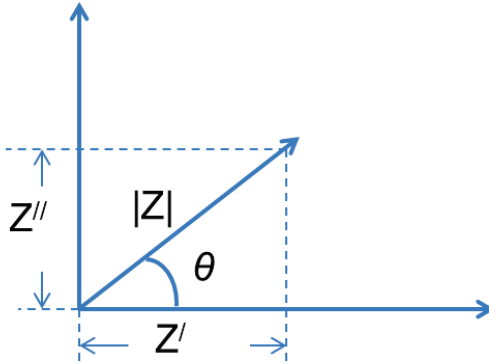
Figure 3-6: Impedance as a planar vector, using polar and Cartesian coordinates.

The real and imaginary parts of the impedance are thus related to the phase angle through

$$Z' = |Z|\cos(\theta) \tag{52}$$

and

$$Z'' = |Z|\sin(\theta) \tag{53}$$

In a Nyquist plot, Z' and Z'' are plotted over a given frequency range, where the phase angle and total impedance at every frequency determines the imaginary and real components. The time constant can be related to the peak angular frequency through

$$\tau = \frac{1}{\omega_p} \tag{54}$$

The double layer and diffusion capacitances arises from τ's sufficiently separated to appear as two distinguishable semi circles in the Nyquist plot, and τ is related to a combination of a capacitor and a resistor through [35]

$$\tau = RC \tag{55}$$

3.5.2 Deconvolution, equivalent circuits and circuit elements

When performing EIS, impedance data are obtained, containing information about specific parts of our measured system. The data are fitted to equivalent circuits, with circuit elements like capacitors and resistors mathematically simulating the dielectric properties of the system. In the following, an overview of the equivalent circuits and elements chosen for the studies included in this work is given.

The relation between the relaxation time constant, resistance and capacitance presented in Equation 55 holds only for a situation where a reaction step has one defined τ. On an electrode surface, there is a radial distribution of reaction sites as well as local currents and potentials, and hence also a distribution of τ's. One must also assume that surface defects and different crystallographic orientations makes the surface nonuniformly active towards adsorbates [35]. Finally, there are numerous ways of interaction between the surface and the different gas phase species, involving surface exchange, red-ox and chemical reactions that are not part of the reaction series described in Tables 3.4-1 and 3.4-2, all giving rise to an even wider distribution of τ's. In deconvoluting the impedance data, this distribution of time constants can be represented by a constant phase element (CPE). The impedance of a CPE can be expressed as

$$Z_{CPE} = \frac{1}{Y_0(j\omega)^n} \tag{56}$$

The values of Y_0 and n are related to the CPE in such a way that Y_0 gives the value of the capacitance of a pure capacitor if $n = 1$. The value of n is related to the phase angle, and for $0 < n < 1$, the CPE yields a pseudo-capacitance (C_p) which can be calculated from

$$C_p = Y_0^{\frac{1}{n}} \cdot R^{\frac{1}{n}-1} \tag{57}$$

There are, however, some limitations to the use of a CPE to represent the sum of electrode surface processes. The first is that the CPE assumes a continuous distribution of τ's. Secondly, and maybe more important for studies of electrode surface reactions, it is only realizable at a finite range of frequencies, as the $\omega \rightarrow 0$ limit for Z_{CPE} does not exist [36]. This implies that surface processes with long relaxation times and low peak angular frequencies are not well defined by the CPE. A multi-step process element like a Gerischer element will be more appropriate in representing these lower frequency reaction steps [37]. A Gerischer element effectively accounts for distributed chemical-electrochemical (CE) reactions [37, 38], and should be well suited, given the variety of interaction possibilities that adds to the electrochemical oxygen reaction on a PCFC cathode. The complex impedance associated with a Gerischer element (Z_G) can, in the simplest form, be calculated according to

$$Z_G(\omega) = \frac{1}{Y_0 \sqrt{k + j\omega}} \tag{58}$$

Here k represents the effective transfer rate for the chemical part of the CE process [39] with units s^{-1}, and Y_0 is for the Gerischer element the electrochemical admittance at $\omega = 1$ rad·s$^{-1/2}$, taking values of S·s$^{-1/2}$. A schematic representation of a Gerischer-like transmission line is shown in Figure 3-7.
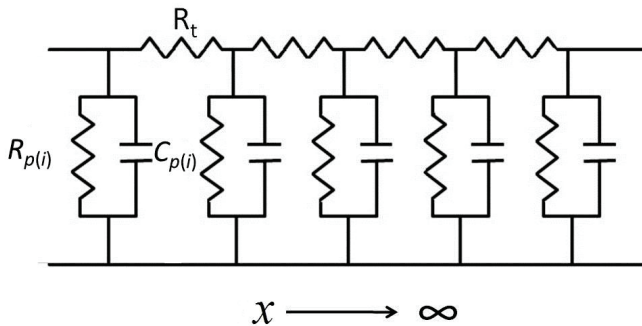

Figure 3-7: Gerischer transmission line with distributed chemical / electrochemical reactions.

The Gerischer element gives a response recognizable in the complex impedance spectrum as a characteristic drop-shaped curve, and at DC, Equation 58 reduces to

$$Z_G^{/}(\omega = 0) = \frac{1}{Y_0 \sqrt{k}} \tag{59}$$

The choice of deconvolution model and circuit elements should be subject to careful considerations, as oversimplifying can give misleading or insufficient information, whereas a more complex model can suffer from correlated parameters or give too many local minima in the iteration process. The representation generally chosen in our studies is based on the Randles-type equivalent circuit [40] with C_{dl} and C_d in parallel, as opposed to the commonly used series of two parallel RC combinations. The Gerischer element is added in series after the Randles circuit in order to account for the low frequency responses.

One challenge encountered when studying the electrode processes, is to account for "leaky current" through the whole measured system [41]. To assume pure ionic conduction in the electrolyte renders that all transport of charge undergoes an electrochemical red-ox process at the electrodes, and implies that the measured data are represented by an equivalent circuit consisting of only one charge carrier pathway. The true situation, however, can easily be such that the transport of charge through the electrolyte is mixed between ionic and electronic species, given measurement conditions. Such a mix of charge carriers will affect the resolved value of the total R_p, as electrons may pass through the whole system without participating in an electrochemical reaction, thereby creating a charge carrier pathway parallel to the electrochemical transfer of charge and mass. Hence, a T, pO_2 or pH_2O dependency can easily be misinterpreted as arising from an electrode process alone when it, in fact, could reflect a relative change in the electronic / ionic conductivity in the electrolyte. In modelling electrode behaviour, this issue is addressed by two different approaches. The simplest way is by representing the total system with an equivalent circuit consisting of a separate electronic rail in parallel to the sum of the circuit elements representing ionic transport (electrolyte) and electrochemical

processes (electrodes). The number of free parameters in the equivalent circuit representation should be limited by applying a fixed ratio between the ionic (R_{ion}) and electronic (R_{el}) resistances in the electrolyte based on separate measurements. The relation between partial and total electrolyte resistances is

$$R_{el.1} = \frac{1}{\dfrac{1}{R_{ion}} + \dfrac{1}{R_{el}}} \tag{60}$$

$R_{el.1}$ is then fitted to the high frequency arc's intercept on the real axis in a Nyquist plot. Figure 3-8 shows the deconvolution model.
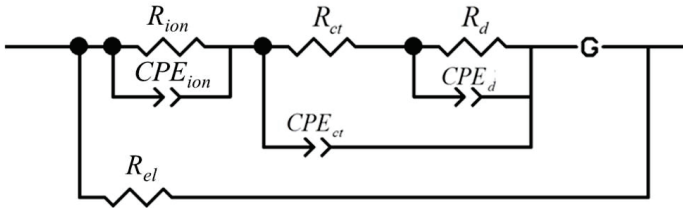

Figure 3-8: Equivalent circuit model based on a Randles-like circuit in series with a Gerischer element and in parallel with an electronic "leaky current" rail.

Another way of handling partial electronic current in the electrolyte is by deconvoluting impedance data without the parallel electronic rail. In this case one must recognize that the measured resistances are in fact parallel combinations of resistances in the electronic and ionic current paths, weighed by their electrolyte partial conductivities. Measured partial resistances are thus only apparent resistances and modelling of the individual charge carrier partial resistances is necessary. In manuscript I, the model shown in Figure 3-8 is used, and in manuscripts III and V, the impedance data are deconvoluted without electronic rail and a novel method for modelling partial resistances in mixed conducting systems is presented.

4.   **Manuscript I**

Development of Proton Conducting SOFCs Based on LaNbO$_4$ Electrolyte – Status in Norway

5. **Manuscript II**

A Pt point contact electrode on proton conducting Ca-doped LaNbO$_4$ studied by impedance spectroscopy and XPS

Manuscript III

Reaction kinetics of protons and oxide ions in $La_{0.8}Sr_{0.2}MnO_3$ / lanthanum tungstate SOFC / PCFC cathodes with and without Pt nanoparticle activation

6.　**Manuscript IV**

La$_2$NiO$_{4+\delta}$ as oxygen electrode on lanthanum tungstate electrolyte

7. Manuscript V

Gd- and Pr-based double perovskite cobaltites as oxygen side electrodes for proton ceramic fuel cells and electrolyser cells.

8. **Summarizing discussions**

In this part the aim is to highlight and discuss the specific objectives assigned in the study of the oxygen electrode. The manuscripts address different topics, but the central objectives might be addressed from different angles throughout the manuscripts. Some results not included in the manuscripts will also be presented here, as they bring additional information and help to put the different parts presented in the manuscript into a larger perspective. What are the characteristics of the reaction kinetics at the proton conductor oxygen electrode, and what demands do these characteristics put on materials properties? What is the role of water in the oxygen red-ox reaction series? How can we optimize the electrode microstructure to facilitate the most efficient reaction path? What are the effects of non-faradaic partial electronic conductivity in the electrolyte and what means of interpretation do we utilize to meet this challenge under various experimental circumstances? And finally: Have we through our investigations been able to present new and promising oxygen electrode materials for proton conducting fuel cells or electrolyzer cells?

8.1 The oxygen red-ox reaction

8.1.1 Rate limiting reaction steps

We have shown through all five manuscripts that the overall oxygen electrode reaction is rate limited by reaction steps at the electrode surface in temperature ranges where protons dominate the charge transport. For the Pt model electrode investigated in manuscript (II), surface diffusion was shown to be rate limiting in the temperature interval 600-700°C. The charge transfer reaction was fast, yielding a low partial resistance, R_{ct}, as compared to the diffusion resistance, R_d. The same diffusion limited behavior is seen for the PCFC reaction on Pt-modified LSM in manuscript (III), though for this system with a somewhat higher relative contribution from charge transfer resistance. The investigations in (III) did not conclude with which of the elementary surface steps that was rate limiting, but there was a gradual shift in apparent activation energy for the rate limiting surface step from high to low

temperatures. This gradual change of Arrhenius' slope is explained by a parallel combination of surface processes with Arrhenius' behaviors and different slopes for reactions associated with transport of protons and oxide ions, where the first dominates at high temperatures and the latter at low. The relative change in charge carriers in the electrolyte over the investigated temperature range will thus give the gradual shift in the slope of the logarithmic plot of combined resistances for protons and oxide ions versus inverse temperature. The proton related surface process on Pt-modified LSM was modelled and fitted to the experimental data with an activation energy of ~90 kJ mol^{-1}. This can be compared to the activation energy of 105 kJ mol^{-1} for OH surface diffusion on Pt obtained in (II). The activation energies for the PCFC surface reactions in (II) and (III) are comparable. Both Pt and LSM are pure electronic conductors in the respective temperature ranges, and the diffusion of oxygen species at the electrode is thus a surface process for both materials. In (II) this diffusion is shown to be via surface hydroxyls. The possible splitting of water and formation of surface hydroxyls on the LSM electrode is not investigated in (III).

The same shift in apparent activation energy over a wide temperature window is also seen for the double perovskite MIEC $BaGd_{0.8}La_{0.2}Co_2O_{6-\delta}$ (BGLC) electrode on BZCY72 electrolyte in manuscript (V). The oxygen reduction reaction on this material is also rate limited by surface processes, especially at temperatures lower than 600°C. BZCY72 is also, like LWO56, a mixed ionic conductor dominated by protons at low temperature. At higher temperatures and under oxidizing conditions, charge transport in BZCY72 is dominated by oxide ions and electron holes. The charge transfer and surface processes for BGLC on BZCY72 are therefore also combinations of SOFC and PCFC reactions. Parallel transport of oxide ions and protons makes it useful to fit each measured partial electrode resistance to a combination of two parallel Arrhenius' type of rate expressions. The PCFC surface reaction, dominating polarization resistance at low temperatures exhibit an activation energy of 50 kJ mol^{-1}. This is about half the activation energies for the PCFC surface reactions on Pt and LSM, suggesting that the surface reaction involving protons on BGLC is easier and faster than on the pure electron conductors.

BGLC is an O-MIEC, and at high temperatures where oxide ions and electron holes dominate the charge transport in BZCY72, charge transfer and diffusion resistances give equal contributions to R_p. The activation energies for the surface processes are lower than for the electrodes in (II), (III) and (IV) both in high temperature SOFC and low temperature PCFC operation. All the O-MIEC double perovskites in (V) exhibit orders of magnitude lower polarization resistances than for the pure electron conducting LSM in (III) and mixed conducting LNiO.

The high temperature reactions in (III), (IV) and V are SOFC reactions and can as such be compared when evaluating the differences between O-MIECs and a pure electron conductor for the oxide ion conducting regime. The mixed conducting LNiO in (IV) has two comparable components of R_p arising from charge transfer and oxygen incorporation. LSM is close to purely electronically conducting over the measured temperature range in (III) and only at the highest temperatures is the electrode reaction affected by the "bulk path" of oxide ion transport through LSM. The activation energy for the SOFC surface reactions on LSM and LNiO in (III) and (IV) is around 150 kJ mol^{-1} for both materials. The reaction mechanisms, however, is most probably different, being surface exchange or surface transport related for the first and oxygen incorporation for the latter.

The double perovskite MIECs in manuscript V all provide fast oxygen kinetics at the electrode surface. The surface related resistance for oxide ions in BGLC is as low as 100 kJ mol^{-1}. In the oxide ion dominated temperature range, R_p is dominated by both charge transfer and diffusion resistance.

To be general, the investigations suggest that the surface reaction of a PCFC cathode exhibits lower activation energy than the surface reaction in an SOFC cathode. So why then the higher polarization in the PCFC-regime?

The results in (III) and (V) suggest attempt rates, i.e., the pre-exponentials of $1/R_p$, increased by orders of magnitude for the high temperature SOFC reactions. In (III), the attempt rates are higher for the SOFC surface reaction only, while the charge transfer reaction exhibits similar (low) attempt rates for protons and oxide ions. This

may be caused by the pure electron conducting LSM, forcing both protons and oxide ions through the tpb only. The surface reaction, on the other hand, is a distributed reaction but only at high temperatures is LSM partly O-MIEC. The partial oxide ion conductivity increases the active surface area and thus also the surface attempt rate as compared to in the PCFC reaction at lower temperatures.

In (V) the attempt rates are orders of magnitude higher for the SOFC charge transfer and surface reactions as compared to the equivalent PCFC reactions. The results indicate that the SOFC reactions are more distributed than the PCFC reactions, probably due to better O-MIEC than P-MIEC properties of BGLC. Hence, a development of microstructure through porous composites or nano structuring is needed to facilitate the PCFC operation.

8.1.2 The effect of ambient water

The first and obvious characteristic of the proton conductor oxygen side electrode reaction is the forming of water from reduced oxygen and protons in cathodic operation, and the oxidation of water to oxygen gas and protons in anodic operation. These reactions are facilitated either on the electrode surface or on the triple phase boundary between gas phase, electrolyte and electrode materials. On a pure electron conducting electrode material, the cathodic and anodic oxygen to water reaction is generally accepted as being a two-proton transfer process at the tpb. Manuscript II suggests a one-proton transfer process at tpb and presents a detailed kinetic model to describe each elementary reaction step in the oxygen reaction on such a pure electron conducting electrode material. This model, along with spectroscopic data, reveals that Pt is catalytically active towards splitting of H_2O at temperatures as low as 700°C, yielding surface hydroxyls that enter the oxygen reaction line. The H_2O produced at tpb is recycled into the oxygen red-ox reaction, acting both as reactant and product. This adds new insight to the universal description of the electrode process on the proton conductor oxygen electrode, where water is present as reaction product.

The effect of water vapor on the oxygen electrode reaction was also measured at high and low temperature in manuscript V. In the temperature range where the ionic current is purely protonic, BGLC on BZCY72 showed increased electrochemical performance when shifting from dry to wet atmosphere at 400°C. In additional measurements not included in manuscript V, $BaPrCo_2O_{6-\delta}$ (BPC) showed the same increase in performance in wet atmosphere at 400°C. In manuscript V we present hydration studies of four double perovskites, where only BGLC showed weight gain upon exposure to ambient water. The results of the dry to wet switch on BGLC and BPC electrodes at low temperature indicate that also for MIEC electrodes, water acts as both reactant and product in the electrode process. This is the case even though hydration is not seen in separate measurements, as in the case of BPC. At higher temperatures, however, water appears to impede the electrode reaction. BZCY72 shows a transition from proton to oxide ion conduction at higher temperatures, and for this electrolyte, the dependency of the electrode reaction rate on ambient water at 650°C is negative for both BPC and BGLC electrodes. Nyquist plots with dry to wet switch for BPC are given in Figures 9-1 and 9-2 for 400 and 650°C, respectively. The sweeps at 400°C are taken at $pO_2 = 1$ atm and the sweeps at 650°C are taken at $pO_2 = 3.8 \cdot 10^{-4}$ atm. The findings in manuscripts II and V conclude that water enhances the electrode reaction for the protonic oxygen-side electrode reaction both for a pure electron conductor, an O-MIEC, and a P-MIEC electrode material. Manuscript V also concludes with water impeding the electrode reaction rate when the ionic current is partly by oxide ions.
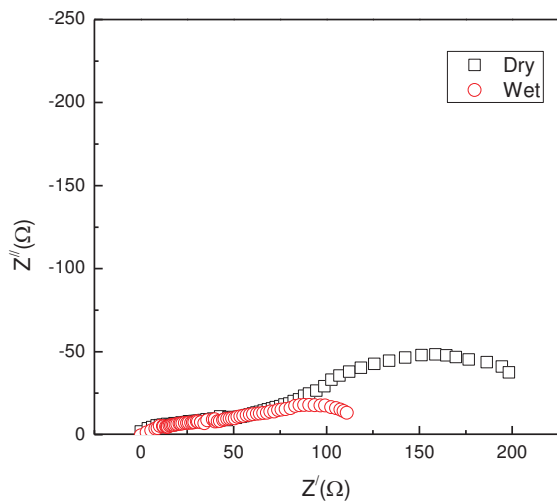
Figure 8-1: Dry to wet switch for the BPC electrode at 400°C and pO$_2$ = 1 atm. Electrolyte resistance is subtracted.
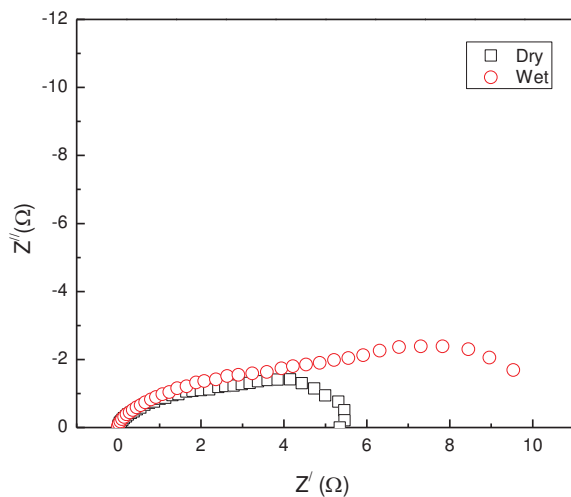

Figure 8-2: Dry to wet switch for the BPC electrode at 650°C and pO$_2$ = 3.8·10^{-4} atm. Electrolyte resistance is subtracted.

8.2 Microstructure

In the four experimental manuscripts (II–V), microstructure is treated in four different manners. In (II), the kinetic model was investigated, and microstructural effects were thus eliminated by applying a model electrode with a defined triple phase boundary length. In (III), Pt nanoparticles were infiltrated in a coarse microstructure, thereby lowering polarization resistance at 650°C from 260 for the non-infiltrated, to 40 Ωcm^2 for the Pt-infiltrated electrode. The aim in (III) was to see the qualitative effect of infiltration, and given the positive effect, an increase of Pt load or the use of alternative oxide nano-sized catalysts such as cobalt oxide might be ways to further optimize the performance.

Manuscript (IV) addresses the well-established method of microstructural improvement by mixing electrolyte and electrode materials in a ceramic-ceramic composite electrode. We tested different ratios of LWO56 / LNiO and compared with the pure LNiO electrode. The results showed that inclusion of the electrolyte phase in the LNiO electrode phase did not lower polarization resistance in this case.

In (V) we applied a functional electrode layer by dripping a suspension of ball-milled MIEC electrode powder onto the sample surface before screen-printing a coarser electrode layer on top. The result was a graded microstructure with a well-sintered, fine-grained functional layer, displaying apparent polarization resistances of 0.05 and 10 Ωcm^2 at 650 and 350°C, respectively. The functional layer can be further optimized with respect to particle size, layer thickness and temperature treatment. The fine-grained suspension can be applied also by spray coating, and the method is thus well suited for up scaling to industrial scale. In the end, infiltration as in (III) in a functional layer as in (V) will give the optimal functionality with respect to microstructure, given the importance of the tpb length for the PCFC oxygen electrode.

8.3 Effect of partial electronic conductivity

In manuscript II, one of the pitfalls that are often overlooked when studying electrode performance is addressed. Many ceramic proton conductors exhibit mixed electronic / ionic conductivity at elevated temperatures and oxidizing conditions, and the non-faradaic flow of electronic charge carriers (current not undergoing a red-ox reaction at the electrodes) in the electrolyte is increasing with temperature and oxygen partial pressure relative to the ionic transport. If this partial electronic conductivity is not handled properly, it can lead to misinterpretations of the governing electrode processes as well as erratic conclusions on electrode performance. Erratic activation energies might in this case be calculated from Arrhenius' plots of $\ln(1/R)$ vs. inverse temperature. When the high temperature current is partly non-faradaic and the low temperature current is purely faradaic, the faradaic part, which is limited by electrode performance, must be treated separately in the interpretations of impedance data, and the non-faradaic current must be seen as running in parallel to the ionic. Under PCFC / PCEC operation, the electronic conduction in the electrolyte is ideally blocked by the reducing conditions at the fuel side, and the electrode polarization will thus be higher than what is seen in pure electrode measurements in oxidizing conditions.

In manuscript II, we present a deconvolution model with a parallel electronic rail used to resolve the partial resistances adding up to the polarization resistance after correcting for partial non-faradaic current. The model gives values for polarization resistance more in accordance with what will be expected under PCFC operation conditions.

In Manuscript III and V we present a more elaborate method for modelling partial polarization resistances in mixed conducting systems. The model enables us to see how the individual charge carriers participate in the polarization of the electrodes and in (V) we see how the non-faradaic current diminishes the polarization when measuring in oxidizing conditions. What can be seen by modelling of partial resistances is that the apparent polarization resistance, measured in oxidizing

conditions is approximately one order of magnitude lower than what will be expected under operation in a PCFC / PCEC at 650°C. At lower temperature, the leaky current is smaller, and the measured results are more in accordance with expected resistances as they would appear under operation.

8.4 Materials

The $BaZr_{1-x-y}Ce_xY_yO_3$ (BZCY) electrolyte is the state-of-the-art material class for PCFCs. MIECs materials such as $Sm_{0.5}Sr_{0.5}CoO_3$ (SSC), $Ba_{0.5}Sr_{0.5}Co_{0.8}Fe_{0.2}O_{3-\delta}$ (BSCF), $La_{0.6}Sr_{0.4}Co_{0.2}Fe_{0.8}O_{3-\delta}$ (LSCF), $PrBa_{0.5}Sr_{0.5}Co_{0.8}Fe_{0.2}O_{5+\delta}$, $GdBa_{1-x}Sr_xCo_2O_{5+\delta}$ and the family of $LnBaCo_2O_{5+\delta}$ (Ln = La, Pr, Nd, Sm and Gd) have all shown good performance on this electrolyte. In Figure 9-3, we compare some of the best reported oxygen electrodes on BZCY / BCY [19, 22, 43] with our reported results for the LSM electrodes in (III), LNiO in (IV) and BGLC in (V). It must be noted here that the values are apparent R_p's only, uncorrected for p-type contributions
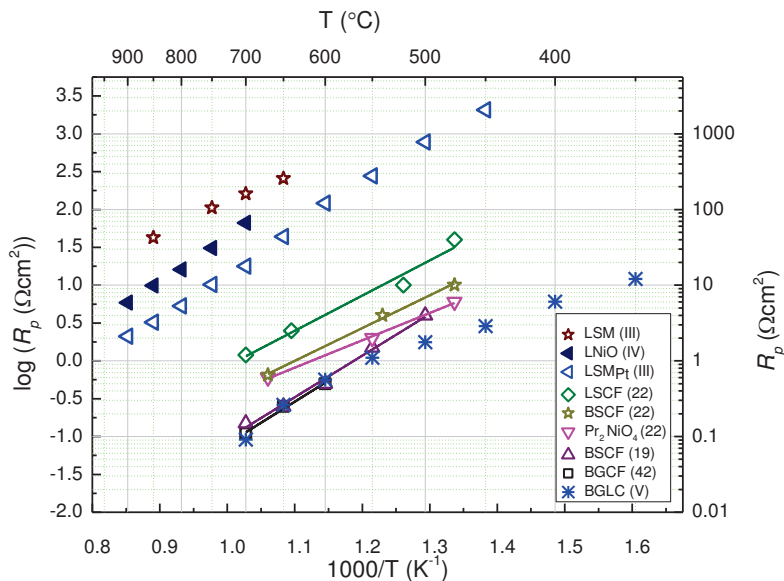

Figure 8-3: R_p vs 1000/T for LSM (III), LSM$_{Pt}$ (III) and BGLC (V) compared with other cathode materials reported for PCFC application.

At 700°C, R_p for BGLC is close to reported values for BSCF and BGCF. Our studies in (V), however does not support such high performance for BGCF. And BSCF has, as earlier mentioned, proven not to be chemically stable. The results for BGLC are, to the best of our knowledge, the best so far for a chemically stable electrode material on a proton conducting electrolyte. The other materials, BPC, BPCF and BGCF, investigated in (V) are also among the best reported materials, though not as good as BGLC. The LSM and LNiO electrodes show much higher polarization, but it must be noted that they are tested on LWO electrolyte. This material exhibits close to pure ionic conductivity, and as shown above, the considerable p-type conductivity of BZCY shifts the polarization down around one order of magnitude as compared to under operation conditions for this electrolyte material. Still, the best MIEC electrodes would outperform even the Pt-impregnated LSM by one order of magnitude also after accounting for the effect of non-faradaic current.

9. **Conclusions**

The investigations have revealed new knowledge on reaction mechanisms, electrochemical properties and materials requirements for the PCFC cathode. The kinetic reactions steps at a pure electron conductor electrode have been described using a Pt electrode on a proton conducting electrolyte. For the first time, the role of ambient water as reactant in the cathodic oxygen reduction reaction is included in the reaction series, where the positive effect of ambient water on the cathodic reaction rate is explained by the formation of surface hydroxyls. The positive effect of ambient water is shown for a pure electron conductor, an O-MIEC and a P-MIEC electrode material on proton conducting electrolytes. The effect on ambient water of the cathode reaction rate is shown to be negative when the electrolyte is mainly oxide ion conducting.

The effect of microstructural improvements on electrode polarization has been shown through infiltration of Pt nanoparticles, and fine-grained powder suspensions have been utilized for functional layer preparation in high-performing electrodes.

A novel model for analyzing mixed conducting systems has been developed, enabling detailed descriptions and modelling of the simultaneous contributions from three types of charge carriers to electrolyte resistance and electrode polarization. The model presents a solution to measurement conditions-induced effect of partial electronic conductivity in the electrolyte, making it possible to model expected real polarization under operating conditions. The model also enables the simultaneous modelling of SOFC-like and PCFC-like electrode reactions in a system of mixed proton / oxide ion conductivity.

New mixed conducting double perovskite materials have been investigated as PCFC / PCEC oxygen electrodes, revealing performances close to- and beyond- state-of-the-art. The highest performing double perovskite material, $BaGd_{0.8}La_{0.2}Co_2O_{6-\delta}$ (BGLC) exhibits a hydration enthalpy of -50 kJ mol^{-1} and an apparent polarization

resistance of 0.05 Ωcm^{-2} at 650°C, and is suggested as a novel proton mixed ionic-electronic conductor (P-MIEC).

The objectives undertaken in the investigations have shown that a well performing PCFC oxygen electrode is within reach, given certain specific improvements. The activation energy of the pure PCFC electrode reaction is most probably sufficiently low, but the pre-exponential values are still too high, and should be lowered by around one order of magnitude. A distributed surface reaction zone will give lower pre-exponentials and thus higher attempt rates and overall performance. This can be achieved through microstructural improvements and/or by enhanced partial proton conductivity in the electrolyte material. BGLC shows P-MIEC characteristics, and the search for improved P-MIECs should be emphasized. Conductivity and thermogravimetric studies, possibly coupled with isotope tracer diffusion studies should be undertaken on mixed conductors with sufficient A-site basicity (for perovskites) to facilitate hydration of native oxygen vacancies. With microstructural improvements, such as infiltration in a porous electrolyte backbone, the series of $BaGd_{1-x}La_xCo_2O_{6-\delta}$ ($0.2 \leq X \leq 1$) might be the new state-of-the-art PCFC oxygen electrode materials.

References

1. Energy, U.D.o. *Energy efficiency & renewable energy \ Fuel Cells \ Distributed / stationary fuel cell systems http://energy.gov/eere/fuelcells/distributedstationary-fuel-cell-systems*. 2013; Available from: http://www1.eere.energy.gov/hydrogenandfuelcells/fuelcells/systems.html.

2. Brett, D.J.L., et al., *Intermediate temperature solid oxide fuel cells.* Chemical Society Reviews, 2008. **37**(8): p. 1568-1578.

3. Kreuer, K.D., *Aspects of the formation and mobility of protonic charge carriers and the stability of perovskite-type oxides.* Solid State Ionics, 1999. **125**(1–4): p. 285-302.

4. Norby, T. and Y. Larring, *Concentration and transport of protons in oxides.* Current Opinion in Solid State and Materials Science, 1997. **2**(5): p. 593-599.

5. Kreuer, K.D., *On the development of proton conducting materials for technological applications.* Solid State Ionics, 1997. **97**(1–4): p. 1-15.

6. Iwahara, H., et al., *Proton conduction in sintered oxides and its application to steam electrolysis for hydrogen production.* Solid State Ionics, 1981. **3–4**(0): p. 359-363.

7. Iwahara, H., et al., *Protonic conduction in calcium, strontium and barium zirconates.* Solid State Ionics, 1993. **61**(1–3): p. 65-69.

8. Shimura, T., S. Fujimoto, and H. Iwahara, *Proton conduction in non-perovskite-type oxides at elevated temperatures.* Solid State Ionics, 2001. **143**(1): p. 117-123.

9. Haugsrud, R. and T. Norby, *Proton conduction in rare-earth ortho-niobates and ortho-tantalates.* Nat Mater, 2006. **5**(3): p. 193-196.

10. Kreuer, K.D., *Proton-conducting oxides.* Annual Review of Materials Research, 2003. **33**(1): p. 333-359.

11. Xia, C., et al., $Sm_{0.5}Sr_{0.5}CoO_3$ *cathodes for low-temperature SOFCs.* Solid State Ionics, 2002. **149**(1–2): p. 11-19.

12. Shao, Z., Haile, Sossina M., *A high-performance cathode for the next generation of solid-oxide fuel cells.* Nature, 2004. **431**: p. 170-173.

13. Sahibzada, M., et al., *Development of solid oxide fuel cells based on a* $Ce(Gd)O_{2-x}$ *electrolyte film for intermediate temperature operation.* Catalysis Today, 1997. **38**(4): p. 459-466.

14. Dusastre, V. and J.A. Kilner, *Optimisation of composite cathodes for intermediate temperature SOFC applications.* Solid State Ionics, 1999. **126**(1–2): p. 163-174.

15. Kim, J.-H., F. Prado, and A. Manthiram, *Characterization of* $GdBa_{1-x}Sr_xCo_2O_{5+\delta}$ $(0 \leq x \leq 1.0)$ *Double Perovskites as Cathodes for Solid Oxide Fuel Cells.* Journal of The Electrochemical Society, 2008. **155**(10): p. B1023-B1028.

16. Choi, S., Yoo, Seonyoung, Kim, Jiyoun, Park, Seonhye, Jun, Areum, Sengodan, Sivaprakash, Kim, Junyoung, Shin, Jeeyoung, Jeong, Hu Young, Choi, YongMan, Kim, Guntae, Liu, Meilin, *Highly efficient and robust cathode materials for low-temperature solid oxide fuel cells:* $PrBa_{0.5}Sr_{0.5}Co_{2-x}Fe_xO_{5+d}$. Sci. Rep., 2013. **3**.

17. Zhang, K., et al., *Synthesis, characterization and evaluation of cation-ordered* $LnBaCo_2O_{5+\delta}$ *as materials of oxygen permeation membranes and cathodes of SOFCs.* Acta Materialia, 2008. **56**(17): p. 4876-4889.

18. Yang, L., et al., *A Novel Composite Cathode for Low-Temperature SOFCs Based on Oxide Proton Conductors.* Advanced Materials, 2008. **20**(17): p. 3280-3283.

19. Lin, Y., et al., *Evaluation of* $Ba0.5Sr0.5Co0.8Fe0.2O3-\delta$ *as a potential cathode for an anode-supported proton-conducting solid-oxide fuel cell.* Journal of Power Sources, 2008. **180**(1): p. 15-22.

20.   Yoo, Y. and N. Lim, *Performance and stability of proton conducting solid oxide fuel cells based on yttrium-doped barium cerate-zirconate thin-film electrolyte.* Journal of Power Sources, 2013. **229**(0): p. 48-57.

21.   McIntosh, S., et al., *Oxygen Stoichiometry and Chemical Expansion of $Ba_{0.5}Sr_{0.5}Co_{0.8}Fe_{0.2}O_{3-\delta}$ Measured by in Situ Neutron Diffraction.* Chemistry of Materials, 2006. **18**(8): p. 2187-2193.

22.   Dailly, J., et al., *Perovskite and A_2MO_4-type oxides as new cathode materials for protonic solid oxide fuel cells.* Electrochimica Acta, 2010. **55**(20): p. 5847-5853.

23.   Tao, S.W., et al., *Electrode materials for intermediate temperature proton-conducting fuel cells.* Journal of Applied Electrochemistry, 2000. **30**: p. 153-157.

24.   Han, J., K. Zheng, and K. Świeczek, *Nickel-based layered perovskite cathode materials for application in intermediate-temperature solid oxide fuel cells.* Functional Materials Letters, 2011. **04**(02): p. 151-155.

25.   Grimaud, A., et al., *Hydration Properties and Rate Determining Steps of the Oxygen Reduction Reaction of Perovskite-Related Oxides as H+-SOFC Cathodes.* Journal of The Electrochemical Society, 2012. **159**(6): p. B683-B694.

26.   He, F., et al., *Cathode reaction models and performance analysis of $Sm_{0.5}Sr_{0.5}CoO_{3-\delta}$–$BaCe_{0.8}Sm_{0.2}O_{3-\delta}$ composite cathode for solid oxide fuel cells with proton conducting electrolyte.* Journal of Power Sources, 2009. **194**(1): p. 263-268.

27.   Ricote, S., et al., *$LaCoO_3$: Promising cathode material for protonic ceramic fuel cells based on a $BaCe_{0.2}Zr_{0.7}Y_{0.1}O_{3-\delta}$ electrolyte.* Journal of Power Sources, 2012. **218**(0): p. 313-319.

28.   NorECs. *NorECs homepage (2014.07.28) http://www.norecs.com/index.php?page=ProboStat*.

29.   Kofstad, P., Norby, T, *Defects and transport in crystalline solids*. Unpublished. 2007.

30.   Nowick, A.S. and A.V. Vaysleyb, *Isotope effect and proton hopping in high-temperature protonic conductors.* Solid State Ionics, 1997. **97**(1–4): p. 17-26.

31.   Tsiplakides, D. and C.G. Vayenas, *Electrode Work Function and Absolute Potential Scale in Solid-State Electrochemistry.* Journal of The Electrochemical Society, 2001. **148**(5): p. E189-E202.

32.   Uchida, H., S. Tanaka, and H. Iwahara, *Polarization at Pt electrodes of a fuel cell with a high temperature-type proton conductive solid electrolyte.* Journal of Applied Electrochemistry, 1985. **15**(1): p. 93-97.

33.   Fleig, J., R. Merkle, and J. Maier, *The pO_2 dependence of oxygen surface coverage and exchange current density of mixed conducting oxide electrodes: model considerations.* Physical Chemistry Chemical Physics, 2007. **9**(21): p. 2713-2723.

34.   Zhao, L., et al., *Reaction model for cathodes cooperated with oxygen-ion conductors for solid oxide fuel cells using proton-conducting electrolytes.* International Journal of Hydrogen Energy, 2012. **37**(1): p. 548-554.

35.   Orazem, M.E. and B. Tribollet, *Electrochemical Impedance Spectroscopy : ECS Series of Texts and Monographs*. 2008.

36.   Barsoukov, E. and J.R. Macdonald, *Impedance Spectroscopy : Theory, Experiment, and Applications (2nd Edition)*. 2005.

37.   Holtappels, P., et al., *Preparation and electrochemical characterisation of supporting SOFC–Ni–YZT anodes.* Solid State Ionics, 2006. **177**(19–25): p. 2029-2032.

38.   Belardi, R.-M., et al., *Electrical study of cathodic activation and relaxation of $La_{0.8}Sr_{0.2}MnO_3$.* Ionics, 2009. **15**(2): p. 227-232.

39.   Boukamp, B.A. and H.J.M. Bouwmeester, *Interpretation of the Gerischer impedance in solid state ionics.* Solid State Ionics, 2003. **157**(1–4): p. 29-33.

40.   Sakurai, K., H. Nagamoto, and H. Inoue, *Microstructure of Pt electrodes over solid-electrolyte and its effects on interfacial impedance.* Solid State Ionics, 1989. **35**(3-4): p. 405-410.
41.   Poetzsch, D., R. Merkle, and J. Maier, *Investigation of oxygen exchange kinetics in proton-conducting ceramic fuel cells: Effect of electronic leakage current using symmetric cells.* Journal of Power Sources, 2013. **242**(0): p. 784-789.
42.   R Strandbakke, V.C., A Zuev, D. S. Tsvetkov, C Argirusis, G Sourkouni-Argirusis, S Prünte, T Norby, *Gd- and Pr-based double perovskite cobaltites as oxygen side electrodes for proton ceramic fuel cells and electrolyser cells.* To be published, 2014.
43.   Ding, H. and X. Xue, *Novel layered perovskite GdBaCoFeO$_{5+\delta}$ as a potential cathode for proton-conducting solid oxide fuel cells.* International Journal of Hydrogen Energy, 2010. **35**(9): p. 4311-4315.